Politecnico di Torino

Politecnico di Torino

Ingegneria Energetica e Nucleare

Sustainable Nuclear Energy

A.a. 2025/2026

Sessione di Laurea Ottobre 2025

Slow Strain Rate Testing of advanced metal alloys in liquid lead doped with tellurium

Relatrice

Prof. Monica Ferraris

Candidato

Federico Mencarelli

Acknowledgements

Vorrei dedicare questo lavoro, che segna la conclusione del mio percorso magistrale, a mia nonna Elsa. Vorrei che fossi qui a goderti questo momento; spero che il mio messaggio d'amore possa comunque raggiungerti.

Desidero innanzitutto esprimere la mia più sincera riconoscenza alla Professoressa Monica Ferraris del Politecnico di Torino, per la supervisione e il prezioso supporto offerti nel corso di questo progetto.

Questa tesi è stata svolta presso il KTH Royal Institute of Technology di Stoccolma. In tale contesto, desidero ringraziare sentitamente tutte le persone che hanno avuto un ruolo fondamentale nel mio percorso. In particolare, il Professor Pär Olsson, mio esaminatore, per i suoi commenti costruttivi e la guida costante durante lo svolgimento del lavoro; i miei supervisori Nils Wikström, Qiuguo Yang, il Dr. Christopher Petersson e il Dr. Peter Szakalos, per il loro continuo supporto, le discussioni stimolanti e l'attenta supervisione. La loro guida è stata determinante per il mio sviluppo, sia accademico che professionale.

L'ambiente del Dipartimento di Ingegneria Nucleare del KTH si è rivelato accogliente, amichevole e inclusivo: un gruppo straordinario di persone, da cui ho tratto numerosi spunti di riflessione e crescita.

Questo lavoro non sarebbe stato possibile senza il supporto finanziario offerto dal KTH e dalla Nuclear Material Platform (NUMAP), per cui esprimo la mia profonda gratitudine.

Un ringraziamento speciale va alla mia famiglia, per l'opportunità che mi ha dato e per il costante sostegno in tutti gli anni di studio. Da Bastia ad Assisi fino a Bastiola, vi voglio bene. Avere una famiglia così meravigliosa è un dono inestimabile: mi considero fortunato ad avervi al mio fianco. Tutto è sembrato più semplice grazie alla vostra

presenza, e il vostro incoraggiamento è stato la mia forza. Un pensiero particolare a mio fratello Michele, per essere stato un modello di resilienza. Ti voglio bene, mamma.

Ringrazio Matilde per avermi sempre sostenuto, soprattutto quando, all'inizio, Torino non sembrava il mio posto e tutto appariva buio e impossibile.

Un ruolo fondamentale l'hanno avuto i miei amici più cari in Italia. Anche se può sembrare un cliché, voi siete la famiglia che ho scelto. La fortuna di avervi nella mia vita è immensa. Non mi sono mai sentito solo: ho sempre percepito la vostra vicinanza. Ringrazio chi mi ha ascoltato senza sosta, come Letizia, e chi ha saputo regalarmi un sorriso anche nei momenti più difficili, come Tommaso, Alessandro e Capretti. Il vostro affetto e la vostra comprensione mi hanno aiutato ad affrontare la distanza. Anche lontani, la vostra presenza ha significato per me il mondo intero.

Un sentito grazie anche ai grandi amici incontrati al Politecnico di Torino. L'inizio è stato tanto difficile quanto arricchente, perché lo abbiamo vissuto insieme. Un'immagine che racchiude tutto è quella di Luigi ed Enrico, fermi davanti allo schermo ad attendere la fine di una simulazione, con un bicchiere di vino in mano. Un ricordo semplice, ma indelebile.

Ultimo, ma non per importanza, un grazie sincero ai colleghi conosciuti nel programma nucleare al KTH, così come a tutti gli amici incontrati in Svezia. Siete stati una costante fonte di ispirazione, supporto e gioia. Le amicizie e i ricordi costruiti resteranno con me per sempre, proprio come l'odore di fumo sui vestiti dopo i tanti falò.

Abstract

As the development of Generation IV lead-cooled fast reactors (LFRs) progresses, ensuring the mechanical integrity of structural materials in harsh core environments is essential, especially under accident scenarios involving fission product release. One such concern is Liquid Metal Embrittlement (LME), a phenomenon where a liquid metal causes a transition from ductile to brittle behavior in structural alloys. This thesis examines the susceptibility of the ferritic alumina-forming alloy Fe10Cr4Al (10-4) to LME when exposed to molten lead contaminated with tellurium (Te), a fission product of particular relevance. Slow Strain Rate Testing (SSRT) is conducted on 10-4 specimens across a range of temperatures, strain rates, and Te concentrations, using both unnotched and notched samples. For reference, 316L stainless steel is tested under similar conditions. Topographic and chemical analysis (SEM/EDS) on 10-4 specimens show that LME is most evident in notched samples, where stress concentration damages the oxide layer that forms on the steel surface, promoting liquid-solid contact. The strongest embrittlement occurs at intermediate Te concentrations (0.3 wt%), where brittle fracture features dominate. Ductility fully recovers at the highest Te content (1.2 wt%), due to the supersaturated solution that leads to the formation of Te-rich precipitates that limit wetting or reduce effective phase interaction. Moreover, LME effects are not observed in unnotched specimens at lower strain rates, suggesting that slower deformation helps preserve oxide integrity and enables the formation of protective precipitates that hinder penetration.

Keywords

Liquid metal embrittlement (LME), Lead, Tellurium, FeCrAl, Slow Strain Rate Test

Sommario

Con l'avanzare dello sviluppo dei reattori veloci raffreddati a piombo di Generazione IV (LFR), garantire l'integrità meccanica dei materiali strutturali in ambienti severi è essenziale, soprattutto in scenari incidentali con rilascio di prodotti di fissione. Una problematica rilevante è l'infragilimento da metallo liquido (Liquid Metal Embrittlement (LME)), fenomeno in cui un metallo liquido induce una transizione da comportamento duttile a fragile nelle leghe strutturali. Questa tesi analizza la suscettibilità della lega ferritica formante allumina Fe10Cr4Al (10-4) all'infragilimento da metallo liquido, esposta a piombo fuso contaminato con tellurio (Te), un prodotto di fissione critico. Sono stati condotti test a bassa velocità di deformazione (SSRT) su provini 10-4 in un intervallo di temperature, velocità e concentrazioni di Te, utilizzando campioni intagliati e non. A scopo comparativo, anche l'acciaio inossidabile 316L è stato testato in condizioni simili. Le analisi SEM/EDS sui campioni 10-4 mostrano che l'infragilimento è più marcato nei provini intagliati, dove la concentrazione di tensione danneggia l'ossido protettivo superficiale, favorendo il contatto tra fase liquida e solida. L'infragilimento maggiore si osserva a concentrazioni intermedie di Te (circa 0.3 wt%), dove prevalgono fratture fragili. La duttilità si recupera alla concentrazione più alta (1.2 wt%) grazie alla formazione di una soluzione sovrasatura e di composti ricchi in Te, che riducono la bagnabilità o l'interazione tra le fasi. Inoltre, non si osservano effetti di infragilimento nei provini non intagliati a basse velocità, suggerendo che una deformazione più lenta preservi l'integrità dell'ossido e favorisca la formazione di precipitati protettivi contro la penetrazione del metallo liquido.

Parole chiave

LME (Infragilimento da metallo liquido), Piombo, Tellurio, FeCrAl, SSRT (Prova a deformazione lenta)

Acronyms

AICRM Adsorption-Induced Reduction in Cohesion Model

BSE Backscattered Electrons

EDE Enhanced Dislocation Emission model

EDS Energy Dispersive Spectroscopy

GFR Gas-cooled Fast Reactor

GIF Generation IV International Forum

LFR Lead-cooled Fast Reactor

LME Liquid Metal Embrittlement

LWR Light Water Reactors

MSR Molten Salt Reactor

RE Reactive Elements

RSE Reduction in Surface Energy Model

SCWR Supercritical Water-cooled Reactor

SEM Scanning Electron Microscope

SFR Sodium-cooled Fast Reactor

SSRT Slow Strain Rate Testing

UTS Ultimate Tensile Strength

VHTR Very High Temperature Reactor

List of Figures

1.1 LFR scheme [8]. 3

2.1 Ellingham diagram showing the Gibbs free energy of oxide formation as a function of temperature for various metal oxides. The red areas indicates the temperature and oxygen partial pressure range where the SSRT tests on 10-4 and 316L were conducted. Adapted from [23]. . . . 7

2.2 Illustration (schematic) of atomic displacements near the crack tip. The bond between atoms A and A_o represents the crack front, while atom B denotes a liquid metal atom interacting with the tip [31]. 14

2.3 Cross section of austenitic PNC 316 stainless steel and ferritic ODS 130 cladding specimens after reaction with liquid Te at 973 K. a) PNC316 SEM image after 10 h exposure, b) ODS 13Cr SEM image after 100 h exposure, c) Te EPMA image for area b), d) Fe EPMA image for area b), e) Cr EPMA image for area b) [14]. 17

2.4 Pb-Rich Region of the Pb-Te Phase Diagram [34]. 18

3.1 Scheme of the SSRT rig [23]. The figure shows, at the bottom, the chamber where the specimen is immersed in the molten metal and subjected to tensile loading. At the top are the traction system, the hermetic sealing for the controlled atmosphere, and the load cell, which records and outputs the force signal. 25

3.2 Specifications of the SSRT sample, given in mm varies by ±0.1 mm [23]. Part of the specimens used do not feature the central notch. 25

3.3 The graph plots oxygen concentration in lead (logarithmic scale) against temperature. It shows stability lines for lead oxyde and iron magnetite oxyde. Experimental conditions are represented, they are located between these lines, tracking closer to the ”Magnetite instability” line [40]. 28

4.1 Stress-strain curves of reference 316L specimens in pure Ar_2. R1 strain rate. 32

4.2 Engineering stress-strain curves of 316L specimens tested at various temperatures in two environments: pure ArH_2 and Pb with 1.2 wt% Te. R1 strain rate. Each pair of curves at the same temperature allows a direct comparison of mechanical behavior under different environmental conditions. 32

4.3 Fracture surfaces show necking formation in the different unnotched 316L samples a) ArH_2 450°C, b) Pb+1.2 wt% Te 450°C, c) ArH_2 500°C , d) Pb+1.2 wt% Te 500°C, e) ArH_2 550°C and f) Pb+1.2 wt% Te 550°C. R1 strain rate. 33

4.4 Stress-strain curves of reference unnotched 10-4 specimens in different enviroments. R1 strain rate. 34

4.5 Fracture surfaces show necking formation in different unnotched 10-4 samples, R1 strain rate in: a) ArH_2 room temperature (23°C), b) ArH_2 atmosphere at 375°C, c) pure Pb at 375°C, and d) pure Pb at 375°C (replicate test). 35

4.6 Stress-strain curves of unnotched 10-4 specimens tested at 375°C in pure lead and in lead with added tellurium. R1 strain rate. 36

4.7 Total final elongation of unnotched 10-4 specimens tested in lead at 375°C with increasing tellurium concentration. R1 strain rate. 37

4.8 Engineering stress-strain curves of unnotched 10-4 specimens tested at various temperatures, R1 strain rate, in two environments: pure ArH_2 and Pb with 1.2 wt% Te. Each pair of curves at the same temperature allows a direct comparison of mechanical behavior under different environmental conditions. 37

4.9 Fracture surfaces show necking formation in the different unnotched 10-4 samples, R1 strain rate tested in: a) pure Pb, b) Pb+0.01 wt% Te, c) Pb+0.1 wt% Te , d) Pb+0.3 wt% Te, e) Pb+0.6 wt% Te and f) Pb+1.2 wt% Te. 38

4.10 Fracture surfaces show necking formation in different unnotched 10-4 samples, R1 strain rate in: a) Pb+1.2 wt% Te 450°C, b) same as a) but zoomed on the red box, c) Pb+1.2 wt% Te 500°C , d) same as c) but zoomed on the red box, e) Pb+1.2 wt% Te 500°C and f) same as e) but zoomed on the red box. Letters ”B” and ”D” respectively mean ”brittle” and ”ductile” fracture appearance. 39

4.11 SEM picture of fracture surface of unnotched 10-4 specimen in ArH_2 at 500°C. R1 strain rate. 40

4.12 Stress-strain curves of unnotched 10-4 specimens in different environments at 375°C. R2 strain rate. 41

4.13 SEM picture of fracture surface of unnotched 10-4 specimens in Pb+Te at concentration a) 0.6%Te and b) 1.2 %Te. Both have been pulled at R2 and 375°C. ”B” and ”D” respectively mean ”brittle” and ”ductile” fracture appearance. 41

4.14 Stress-strain curves of reference notched 10-4 specimens. R1 strain rate. 43

4.15 Stress-strain curves of notched 10-4 specimens at different Te concentrations. R1 strain rate. 43

4.16 Total final elongation of notched 10-4 specimens tested in lead at 375°C with increasing tellurium concentration. R1 strain rate. 44

4.17 Fracture surfaces show necking formation in the different notched 10-4 samples, R1 strain rate in: a) pure Pb, b) Pb+0.01 wt% Te, the red box shows a probable brittle fracture feature, c) Pb+0.3 wt% Te , d) Pb+0.8 wt% Te, e) Pb+1.2 wt% Te and f) same as e) but zoomed on the red box. ”B” and ”D” respectively mean ”brittle” and ”ductile” fracture appearance. 45

4.18 BSE-SEM images of an unnotched specimen tested in Pb + 1.2 wt% Te at 375°C, R1 strain rate. In a), the overall fracture surface is shown, while b) presents a close-up view. 46

4.19 EDS analysis of 316L tested in Pb + 1.2 wt% Te at 550°C. (a) SEM close-up of the fracture surface showing a high concentration of precipitates. (b) Corresponding atomic% composition at the labeled points. 47
4.20 EDS map of close up on lead-tellurium precipitates of 10-4 unnotched sample tested in Pb+1.2 wt% Te at 375°C. 48
4.21 Solution precipitates observed in the area surrounding the specimen after opening the rig following the test of the notched sample in Pb+1.2 wt% Te. 49

5.1 Engineering strain at fracture, normalized to the pure lead reference value, as a function of Te concentration for notched and unnotched specimens. 52
5.2 Schematic close-up of the SSRT rig and the formation of a precipitate barrier around the specimens, represented by the yellow area. Original picture from [23]. 53

A.1 Close-up of the specimen halves reassembled after the test, ready for measurement. 63

List of Tables

3.1 Chemical composition of 10–4 and 316L alloys in wt%. 24
3.2 Comprehensive list of all tests performed, including experimental conditions. The columns include the test identification code, the presence or absence of a notch, the test environment conditions (i.e., presence or absence of lead and tellurium), the reference test temperature, and finally the strain rate used. 30

Contents

1 Introduction **1**

1.1 Background and Motivation 1
1.2 Problem Statement 4
1.3 Research Objectives 4
1.4 Research Significance 5
1.5 Outline 5

2 Background **6**

2.1 Alumina Forming Steels 6
2.2 Material Science Basic 8
2.2.1 Surface Energy 8
2.2.2 Brittle Fracture 8
2.2.3 Ductile Fracture 9
2.2.4 Adsorption 10
2.3 Liquid Metal Embrittlement (LME) 11
2.3.1 Phases Contact 11
2.3.2 Factors Affecting Susceptibility to LME 12
2.3.3 Fundamental Theories Explaining LME 13
2.4 Tellurium 15
2.4.1 Related Work 15
2.5 Solute control 17
2.5.1 Activity 19
2.5.2 Oxygen Concentration in Liquid Phase 20
2.6 Related Work 21
2.7 Basis for the Present Work 21

3 Materials and Methods **23**

3.1 Materials 23

3.1.1 Lead . . . 23
3.1.2 Tellurium . . . 23
3.1.3 FeCrAl . . . 23
3.1.4 Stainless Steel 316L . . . 24
3.2 Slow Strain Rate Testing Rig . . . 24
3.3 Methodologies and Experimental Parameters . . . 26
3.3.1 Experimental Procedure . . . 26
3.3.2 Experimental Parameters and Variable Control . . . 26
3.3.3 Overview of Performed Tests and Rationale . . . 28
3.4 Analysis and Characterization . . . 29

4 Results **31**
4.1 Unnotched Samples . . . 31
4.1.1 316L Samples . . . 31
4.1.2 10-4 Samples . . . 34
4.2 Notched Samples . . . 42
4.3 Precipitates . . . 46

5 Discussions and Conclusions **50**
5.1 Discussions . . . 50
5.1.1 LME on Notched and Unnotched 10-4 . . . 51
5.1.2 LME on Unnotched 10-4 at Slowest Strain Rate R2 . . . 53
5.1.3 LME on 316L . . . 54
5.1.4 Limitations of the Study . . . 54
5.2 Conclusions . . . 55
5.2.1 Future Work . . . 55
5.2.2 Final Words . . . 56

References **57**

Chapter 1

Introduction

1.1 Background and Motivation

The pressing challenge of increasing global temperatures and climate change necessitates a rapid transition towards energy sources that produce low or zero greenhouse gas emissions. Currently, a large portion of the world's energy supply relies on fossil fuels, which significantly contribute to carbon emissions. As global energy demand is projected to increase substantially, particularly in developing countries, finding clean, safe, and cost-effective energy solutions is crucial for ensuring the sustainability of [1].

Nuclear energy is presented as a competitive and mature low-carbon technology that currently operates at very high levels of safety. It provides a significant portion of the world's electricity, offering a non greenhouse-gas emitting source and contributing to a more stable and secure energy mix through diversification [2][1][3]. The renewed interest in nuclear energy, sometimes referred to as a "nuclear renaissance," is driven mainly by concerns over climate change, security, independence of supply, and energy costs [4].

Most of the nuclear power plants currently in operation are Light Water Reactors (LWR) [5]. While LWRs provide a secure and cost competitive electricity supply in many markets [6], concerns exist regarding the long-term availability of fuel resources for a massive expansion of nuclear power using existing technology. The current technology primarily relies on the fission of U-235, which constitutes only about 0.7% of natural uranium. Estimates suggest that readily available uranium resources,

based on current consumption rates and operating reactors, could be exhausted by the middle of this century, emphasizing the need for more sustainable technologies [3]. Expanding nuclear capacity significantly would require a large increase in uranium mining capacity, which is noted to face challenges in keeping up with demand, and the overall economically feasible uranium resources are considered insufficient for a massive, long-term expansion with current reactor types[7][2].

To address fuel shortages and other limitations, and to broaden the opportunities for nuclear energy's future role, next-generation systems known as "Generation IV" are being developed through international collaborative efforts. The Generation IV International Forum (GIF), established in 2001, aims to establish the viability of new nuclear energy system concepts to meet future needs for clean and reliable energy, including non-traditional applications beyond electricity generation. The ambitious goals for Generation IV nuclear energy systems are defined in four broad areas: sustainability, economics, safety and reliability, and proliferation resistance and physical protection. The generaiton-IV systems are intended to provide sustainable energy generation that meets clean air objectives and provides long-term availability of systems and effective fuel utilization for worldwide energy production. They also aim to minimize waste and the long-term stewardship burden, offer competitive life-cycle costs with comparable financial risk to other energy projects, excel in safety and reliability, potentially eliminating severe accidents, and meet stringent standards for proliferation resistance and physical protection. The development effort involves selecting the most promising concepts and conducting extensive research and development [3].

The Lead-cooled Fast Reactor (LFR) is one of these six Generation IV concepts and its scheme is shown in Figure 1.1. It features a fast neutron spectrum, operates at high temperatures, and uses molten lead or Lead-Bismuth Eutectic (LBE) as coolant. Lead/LBE are described as a low-pressure, chemically inert liquids with very good thermodynamic properties as well as the ability to act as a neutron shield. LFRs are expected to have multiple applications, including the production of electricity, hydrogen, and process heat. A key advantage of the LFR operating in a fast-neutron spectrum is its excellent materials management capabilities and the use of a closed fuel cycle for efficient conversion of fertile uranium. Fast reactors, in general, play a unique role in actinide management as their high-energy neutrons are more effective at fissioning actinides. The LFR can be used to consume actinides from spent LWR

fuel and can also function as a burner/breeder with thorium matrices. This capability to utilize fissile material more efficiently and manage waste effectively contributes significantly to the sustainability goals of Generation IV systems, potentially increasing the available fuel resources by a factor of 100 and extending the viability of nuclear energy for thousands of years, even with increased capacity [3].

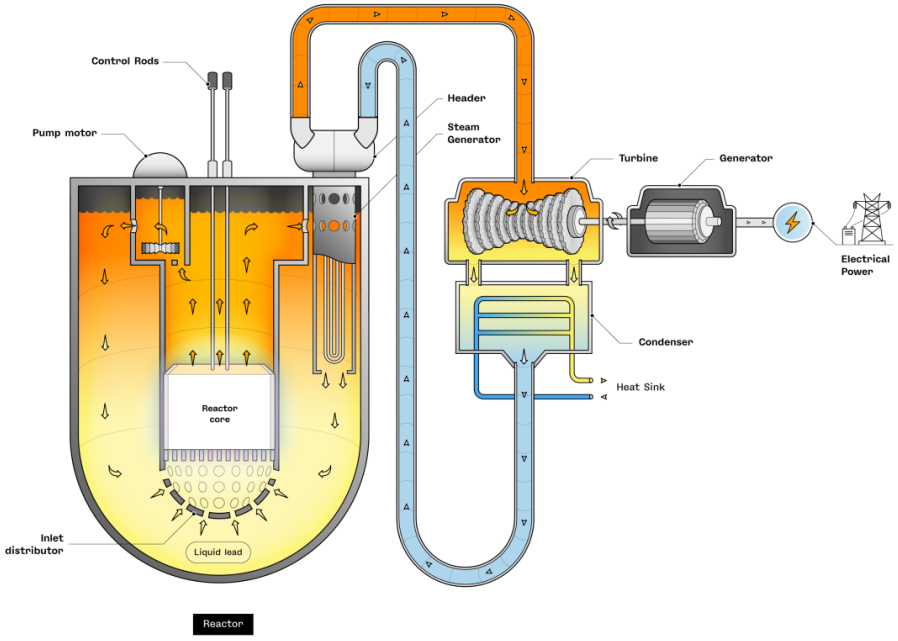

Figure 1.1: LFR scheme [8].

However, there are different perspectives on the timeline and feasibility of commercially deploying advanced reactor types like LFRs. Widely accepted predictions indicate that fast reactors may not be available for commercial deployment before 2030 [8], and it is even doubtful if a commercially deployable version will be ready by then, given the research effort needed. Past experimental or demonstration LFRs have shown challenges, such as low load factors and issues with sodium coolant leaks and fires in sodium-cooled designs [3][9]. The development of LFR, as for the other Gen IV reactors concepts, presents significant engineering challenges, particularly in the selection of structural materials capable of withstanding extreme operating conditions.

In this study, the ferritic alumina-forming Fe10Cr4Al steel (10-4) is investigated as a promising candidate for coating previously tested cladding materials. The steel behavior under conditions where the lead coolant is contaminated by the fission product tellurium (Te) has been studied, since the release of Te from the fuel cladding during accident scenarios may threaten the integrity of cladding materials. Tellurium

is of particular concern because, if released into the liquid lead coolant, it could interact with the coatings on adjacent fuel rods' cladding, potentially compromising their mechanical integrity. A well-known phenomenon linked to such interactions is LME, where certain liquid metals cause structural steels to become brittle and fail prematurely under mechanical stress. This phenomenon has been observed across various metal–liquid metal systems. Although several previous studies have examined tellurium effects in different steel alloys [10]–[15], these have largely focused on general corrosion mechanisms rather than LME specifically. Moreover, there remains a significant lack of data regarding the effects of tellurium on FeCrAl alloys, which are among the candidate materials for next-generation reactor systems.

1.2 Problem Statement

The presence of tellurium in liquid lead environments poses significant concerns about the reliability of 10-4 steel as a potential cladding coating for Lead-cooled Fast Reactors (LFRs). Specifically, it is unclear:

- At what concentrations tellurium becomes detrimental to steel performance.
- How tellurium influences embrittlement mechanisms.
- Whether the embrittlement effect significantly deviates steel properties from their intended operational conditions.

Understanding these aspects is essential to assess the suitability of 10-4 for LFR environment and to establish acceptable limits for tellurium contamination in lead coolants.

1.3 Research Objectives

This study aims to:

1. **Investigate the occurrence of LME** in 10-4 steel under the studied conditions.
2. **Determine the critical tellurium concentration threshold** beyond which the steel properties are significantly affected.

To achieve these objectives, a series of Slow Strain Rate Testing (SSRT) will be conducted on steel specimens immersed in liquid lead containing varying amounts of dissolved tellurium. The mechanical response of the material will be correlated with the tellurium concentration to assess its influence on embrittlement behavior and identify possible LME phenomena.

1.4 Research Significance

This investigation contributes to the *materials science and nuclear engineering fields* by providing new insights into the behavior of 10-4 steel in tellurium-contaminated liquid lead environments. The findings will:

- Support the **design and selection of advanced materials** for lead-cooled Generation IV reactors.
- Enhance the understanding of **failure mechanisms in nuclear structural components**.
- Provide experimental data to refine **safety assessments for accident scenarios** in lead-cooled reactors.

1.5 Outline

This thesis is structured as follows:

- **Chapter 2** provides both the general *engineering background* required to address the proposed topic, focusing on LME mechanisms, steel–liquid metal interactions, and a review of the most relevant literature. This helps the reader grasp the specific issues addressed in this work, highlighting key studies and outlining prior research that this thesis builds upon.
- **Chapter 3** describes the *experimental methodology*, including SSRT conditions, sample preparation, and analysis techniques.
- **Chapter 4** discusses the *experimental results*, focusing on specimens mechanical behavior and fracture analysis.
- **Chapter 5** provides the *discussion and conclusions*, summarizing key findings, identifying limitations, and suggesting future research directions.

Chapter 2

Background

2.1 Alumina Forming Steels

In environment such molten lead or lead-bismuth eutectic materials have to withstand very harsh and challenging conditions [3]. Specifically, a high corrosion resistance is required, along with good mechanical properties and workability for the production and joining of components. Available materials including ferritic–martensitic steels (T91, HT9) and austenitic stainless steels (Grade 316L) has proven excellent capabilities in such situations. However, austenitic stainless steels are susceptible to a severe corrosion attack by the LBE at temperatures above 500°C due to the presence of a high content of Ni that has a wide solubility in liquid lead alloys. On the other hand, ferritic-martensitic steels develop thick oxide layers under similar conditions, which limits their use to lower-temperature environments (below 500°C) due to the reduced thermal conductivity caused by the oxide layer thickness [16], [17].

Alumina-forming ferritic alloys are well known for their interesting corrosion resistance in liquid lead at high temperatures, creating a stable, thin and slow growing protective alumina scale. One of the most important features of aluminium is that this element sits very low in the Ellingham diagram, as shown in Figure 2.1, which plots the standard Gibbs free energy of formation of oxides as a function of temperature. This position indicates that the formation of its oxide (i.e., alumina) is thermodynamically much more favourable and stable compared to the oxides of the main alloying elements in steels. The typical content of chromium in commercial FeCrAl alloys is typically high, around 15–22 wt% specifically, as well as high content of aluminium (4.5–5.5

wt%), together they contribute to excellent oxidation resistance of the steel. The drawback of such high chromium content is the susceptibility of ferritic structure to spinodal decomposition at approximately 475°C. At this temperature, the material undergoes rapid phase separation into an iron-rich phase (α) and a chromium-rich phase (α'), leading to significant embrittlement [18][19][20]. Additionally, their high level of aluminium leads to poor workability and weldability [21]. Nevertheless, previous studies have shown that these drawbacks can be mitigated by reducing the chromium and aluminium contents to 10 wt% and 4 wt%, respectively, while still maintaining good corrosion resistance. In such a case, they have been shown to form a protective oxide layer in liquid Pb environments up to 750 °C [22].

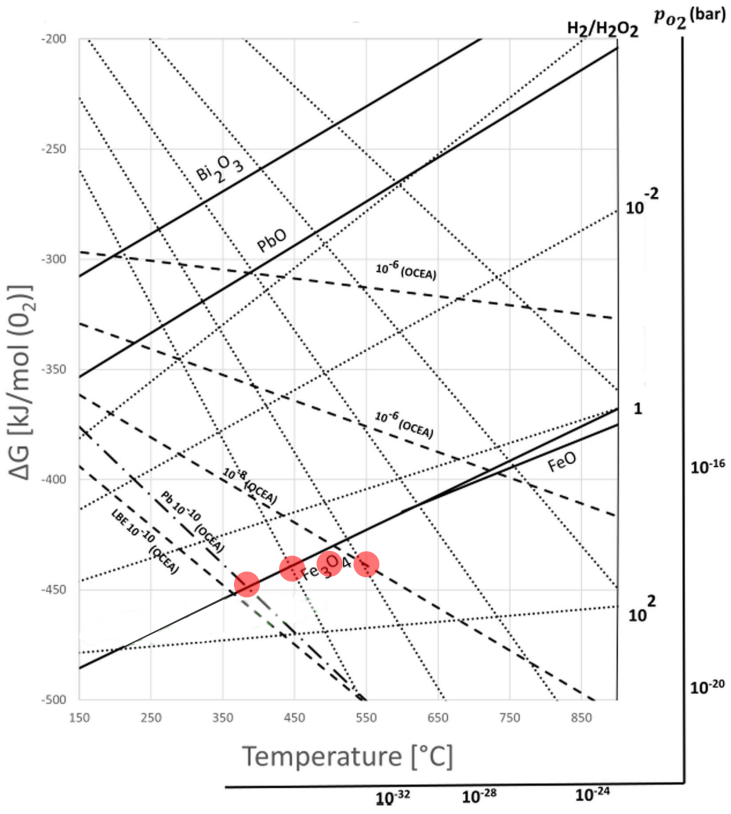

Figure 2.1: Ellingham diagram showing the Gibbs free energy of oxide formation as a function of temperature for various metal oxides. The red areas indicates the temperature and oxygen partial pressure range where the SSRT tests on 10-4 and 316L were conducted. Adapted from [23].

2.2 Material Science Basic

2.2.1 Surface Energy

The surface energy of solids can be thought of as being similar to the surface tension in liquids. It represents the reversible work needed to create a unit area of surface while maintaining constant temperature and pressure. In a solid, forming a new surface involves breaking the bonds between atomic layers, which is why surface energy is always a positive value [24].

When a surface is cut, the energy used in the process is stored in the newly created surfaces. As a result, the particles on the surface store more energy than those in the bulk [25]. This can be explained by the fact that, without this energy difference, there would be nothing preventing bulk particles from becoming surface particles. In other words, without this energy step, there would be no reason for the material to maintain its shape, nor for the bulk material to separate, sublime, and create additional surfaces. Therefore, an energy threshold must be overcome for a bulk particle to transition into a surface particle.

2.2.2 Brittle Fracture

Brittle fracture is the process by which certain materials fail in service, exhibiting very limited deformation and consequently storing significantly less energy compared to ductile materials. There is no advance warning, and the consequences can be catastrophic. Once crack propagation begins, the minimal plastic deformation available does not significantly reduce the load acting on the component. As a result, the stress continues to increase due to the progressively reduced cross-sectional area supporting the load. Materials can be intrinsically brittle or may become temporarily or permanently brittle after exposure to specific environments. Factors contributing to this behavior include hydrogen embrittlement, radiation damage, and the presence of liquid or solid metals.

In a generic brittle fracture, distinctive river lines can often be observed. These formations indicate the direction of crack propagation, helping to identify the fracture initiation site, whether it originates from a defect, a stress concentration, or another contributing factor.

The fracture mechanism can follow two primary modes: intergranular and transgranular. In the former, the crack propagates along the grain boundaries, while in the latter, it cuts through the grains themselves. Often, brittle fracture results from a combination of both mechanisms rather than being purely one or the other.

Intergranular fracture propagation was more common in old steels since the average grain size was bigger and bonds between grains themselves weaker because of higher sulfur levels. At high magnification, brittle fractures exhibiting intergranular propagation reveal the flat facets of individual grain crystals, oriented at various angles. The blocky appearance of these grains is distinctly visible, facilitating the identification of their shapes and sizes along the fracture path.

Transgranular fracture propagation is the most common way; when brittle fracture occurs in this way, the fracture surface appears faceted under a microscope, with the fracture facets typically cutting through the grains. On these microscopic fracture planes, microscopic river lines can be observed in addition to the macroscopic ones that can be observed in any generic brittle fracture, they point toward the fracture initiation site. If the initiating defect is not immediately apparent through visual inspection, microscopic analysis can often reveal it. The appearance of the fracture is mostly dull, especially when compared to the shinier look of intergranular fractures [26].

2.2.3 Ductile Fracture

Ductile fracture describes the process where a material fails after undergoing significant plastic deformation beyond its yield limit. This stands in contrast to brittle failure, which exhibits little to no plastic deformation or reduction in cross-sectional area before fracture. The process of ductile failure is multi-staged, particularly under tensile loading. Initially, the applied tensile stress exceeds the material's elastic limit, leading to plastic deformation. This deformation is often accompanied by ”necking,” a localized reduction in the cross-sectional area of the part. Subsequently, internal defects, pre-existing pores, voids, or inclusions within the material act as nucleation sites for microvoids. These microvoids then grow and coalesce, meaning they join with nearby voids to form larger discontinuities. Finally, a crack propagates from these larger discontinuities until the material separates. Under a Scanning Electron Microscope (SEM), the surface of a ductile fracture exhibits a distinctive appearance characterized by numerous ”dimples”. These dimples are small, hemispherical or

elongated cavities, which are the morphological signature of the microvoid coalescence mechanism. A higher degree of ductility in the material is often correlated with more pronounced necking, leading to a sharper point in the fracture area [27][28].

2.2.4 Adsorption

Adsorption is a surface phenomenon in which atoms, ions, or molecules (collectively called the adsorbate) from a gas, liquid, or dissolved solid adhere to the surface of another substance, known as the adsorbent. This process involves the accumulation of the adsorbate on the surface without it diffusing into the bulk of the adsorbent; this is the key difference between adsorption and absorption. Moreover, adsorption may involve chemical interactions such as Van der Waals forces or covalent bonds [29].

Physisorption

Physisorption, or physical adsorption, refers to the buildup of adsorbate molecules on a solid surface due to weak Van der Waals forces. The process generally diminishes with increasing temperature, and the adsorbed molecules are not dissociated. It is non-selective, as Van der Waals forces are universal, and reversible, with adsorption varying by pressure. The extent of adsorption increases with the surface area [29].

Chemisorption

Chemisorption, or chemical adsorption, occurs when adsorbate atoms or molecules are bound to a solid surface by covalent or ionic bonds. Unlike physisorption, it can involve dissociation of the adsorbed molecules. It is highly specific and only occurs when chemical bonding is feasible. While it also increases with surface area, chemisorption is characterized by a significant enthalpy due to bond formation and is usually irreversible. It modifies the electronic structure of the adsorbate [29].

2.3 Liquid Metal Embrittlement (LME)

LME is a phenomenon where a ductile material shows brittle fracture modes and loss of tensile ductility when exposed to specific liquid metals. However, liquid-metal environments generally do not affect yield stresses or strain-hardening rates [30]. One of the most interesting aspects of liquid metal embrittlement is its selectivity. It is often said that only certain liquid metals can embrittle specific solid metals [31].

Ideally, an experimental technique that aims to understand the atomic reasons of LME should be capable of detecting any variation in electron distribution in the surface bonds, which may lead to weakening without applying a stress. However, since such an effect would be confined to the immediate surface layer of atoms, it would not be easily observed in studies involving changes in the physical properties of the specimen as a whole. Therefore, it is advisable to adopt experimental techniques that aim to determine the bond strength at the crack tip of the solid and the general behaviour in the presence of adsorbed liquid metal species [31].

In general, the appearing of a fracture induced by LME look the same as a general brittle fracture. After the component failure, the metal responsible for LME can sometimes be visually identified on the crack tip. It is characterized by the presence of either a solidified film on the fracture surface or globules deposited in the same area. However, it is important to consider all potential reactions or the formation of intermetallic compounds that may have occurred during or prior to the fracture [32].

2.3.1 Phases Contact

The embrittlement can occur either during the fabrication of the component or during service, provided that close contact between the material and the liquid metal is established, with no oxide film preventing this interaction [32]. Low solubility between two metals promotes better wetting. However, embrittlement only occurs occasionally when the metals exhibit such low mutual solubility that they form immiscible phases upon melting. However, it remains well-established that the liquid must closely adhere to the solid surface to trigger embrittlement and must also be present at the crack tip to propagate failure. Despite this high intimacy, in most cases of LME, poor or no penetration of liquid metal into the solid metal has been observed [31].

Embrittlement by liquid metals can also occur by corrosion, or by diffusion-controlled intergranular penetration processes. Such time- and temperature-dependent processes, however, are not considered either responsible or necessare for the occurrence of liquid metal embrittlement in most cases [30][31]. As consequence, if the specimen is pre-exposed to ensure complete wetting, but is then removed and cleaned of the liquid metal, LME does not occur, even if diffusion has taken place [32], in other words ”LME does not cause a permanent change in the solid metal” [23].

2.3.2 Factors Affecting Susceptibility to LME

Is well established that LME is likely a special case of brittle fracture and that prerequisites for its occurrence are the same as those for brittle fracture. The factors that control and influence the phenomenon can be broadly divided into two categories. The first includes all aspects related to the chemical interaction between the liquid and solid phases, which determine whether a given metal pair is theoretically susceptible to LME. The second category covers the physical and metallurgical conditions that, if LME is possible, govern how and where brittle cracking initiates and propagates under different stress and environmental conditions [31].

Microstructure

Regarding the second category factor, several microstructural effects influencing susceptibility to LME are commonly observed across various materials. These effects include: (1) an increase in LME susceptibility with larger grain sizes, (2) a greater tendency for LME in materials exhibiting planar slip rather than wavy slip, and (3) a reduction in LME susceptibility with increasing levels of cold work [31][32].

Temperature and Oxygen Level

Susceptibility to embrittlement is generally highest when the temperature is near the melting point of the embrittling metal, and it tends to decrease as the temperature moves either above or below that point [30]. The decrease in embrittlement with rising temperature in many cases could be linked to the accelerated surface reactions of the adsorbate, such as desorption, compound formation, or dissolution, which may shorten the adsorbate’s residence time on the surface [30].

The amount of oxygen in the molten metal influences the extent and occurrence of LME, as it regulates the potential formation of a protective oxide layer. The presence of this layer prevents direct contact between the two metals, inhibiting wetting, which is a fundamental prerequisite for LME to occur, as mentioned in 2.3.1.

2.3.3 Fundamental Theories Explaining LME

Reduction in Surface Energy Model (RSE)

Several work have suggested that LME is connected with a reduction of the surface-free energy of the solid metal by the adsorbing liquid metal species or with the surface tension at the interface between the solid and the liquid metal. Effects of embrittlement have to be initiated at the interface between the solid and the liquid metal and therefore interface energy considerations have to play a crucial role. However, the experimentally measured values of total energy involved in crack growth are often several orders of magnitude larger than the surface energy of the solid. The above hypothesis fails to suggest any mechanism by which the plastic part of the surface energy can be minimized so that brittle crack growth will be made possible in a ductile solid in a liquid metal medium. In other words, such a thermodynamic treatment is not very illuminating on the mechanism of LME at an atomic or an electronic level[31].

Adsorption-Induced Reduction in Cohesion Model (AICRM)

This model is based on the effect that the adsorption of molten metal at the fracture tip reduces the cohesion of the material's atoms [31], as schematized in Figure 2.2. The effect of adsorption in metals is at maximum limited to just one or two atomic distances because the high electron density in metals prevents any significant influence at greater depths [32]. The liquid metal weakens the bonds, lowering the maximum load, and it may happen spontaneously or during loading of the material. In the latter case, the crack propagation will preferentially occur at points where there are stress concentrations, both microscopic and macroscopic, caused by the component's processing. However, the process depends on how the molten metal reaches the fracture tip, and that is happening by capillary flow [33]. It can be hypothesized that the molten metal keeps up with the propagating crack tip [31].

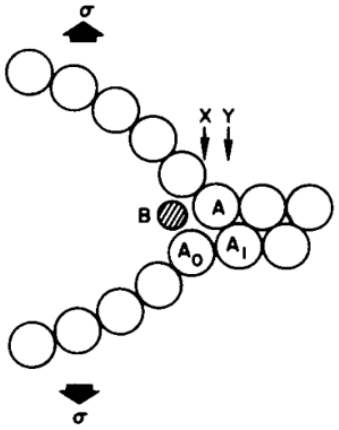

Figure 2.2: Illustration (schematic) of atomic displacements near the crack tip. The bond between atoms A and A_0 represents the crack front, while atom B denotes a liquid metal atom interacting with the tip [31].

Enhanced Dislocation Emission model (EDE)

In accordance with the previous model, this theory also attributes the cause to the adsorption of the liquid metal at the crack tip; however, the effects are different. This model was proposed by Lynch [32][30], who, based on numerous in-depth metallographic and fractographic analyses of LME, suggests that the reduction in strain is due to a decrease in shear strength. The decrease is caused by chemisorption, which promotes the injection of dislocations at the crack tip, leading to crack growth through a more localized microvoid coalescence process compared to what occurs in inert environments. In other words, adsorption facilitates the nucleation of dislocations at crack tips, crack growth in liquid metal environments occurs then by slip rather than tensile decohesion at crack tips.

The adsorptive effect upon the nucleation of dislocations at crack tips is to be expected on theory: the atomic arrangement in the outermost layer of clean metal surfaces is usually like that of adjacent parallel planes within the interior of the crystal, but in some crystal faces there tends to occur a slight contraction in the atoms' radial distance between them. This non-uniformity of the surface lattice would prevent the nucleation of dislocations since dislocations within the outermost few layers would be accompanied by extra-normal distortions of the lattice. In this case, the effects of adsorption upon such surface features will be a function of the mode of adsorption:

- Physical adsorption should not significantly affect the surface characteristics since there is no electronic interaction between adsorbate and adsorbent.
- Strong chemisorption tends to cause environmental atoms to become included in the outermost layer of the metal atoms. Such surface lattice disruption and the development of strong directional bonds between the atoms of the adsorbate and adsorbent should prevent rather than promote dislocation nucleation. Furthermore, this effect tends to cause incipient compound or other immiscible phases to be formed that could have the above-mentioned effect; this would be consistent with that expressed in 2.3.1 concerning metals couples compatibility.
- Weak chemisorption is able to frame the surface atoms in a manner to decrease the 'surface-lattice distortion' and to promote the nucleation of dislocations. That is, donation of electrons by weak chemisorbed environmental atoms to metal atoms at the surface may raise the density of electrons in a localized area, enhance the mutual repulsive force of surface atoms and weaken the shear strength of interatomic bonds at surfaces.

2.4 Tellurium

Inside a nuclear reactor, the quality of a cladding material is also evaluated based on its resistance to corrosion by fission products. In fact, reactions between fission products and the cladding represent one of the key phenomena that can limit the cladding's service life in a power plant. Among the various fission products released from the fuel, tellurium and cesium are considered the most detrimental.

Tellurium melts at 450 °C and can exist in liquid form at the operating temperatures typically found at the cladding surface. Among all fission products, cesium, iodine, and tellurium are known to cause significant and potentially hazardous interactions with the fuel pin cladding. The remaining fission products are either non-reactive or generated in quantities too small to have any meaningful impact on the cladding.

2.4.1 Related Work

In [12], it was shown that volatile fission products such as tellurium, iodine, and cesium can significantly contribute to the oxide-cladding reaction in fast reactor fuel, primarily through their dechroming effect on 316L stainless steel. Key influencing factors include

fuel stoichiometry deviation, internal cladding temperature, and radiation-enhanced diffusion.

However, in [15], it was demonstrated that the reaction of Te with steels is relatively independent of the oxygen content. This study focused on the effects of fission products on 316L. At low oxygen levels, Te attacks the steel directly; at higher oxygen potential, since chromium has the greatest affinity to oxygen among the three main components of austenitic steels, a chromium oxide scale forms first. This scale protects the cladding from Te attack. However, this protective role can be compromised when Cs and I interact with the cladding, initiating a simultaneous corrosion attack by all fission products. The study showed that at low temperatures, corrosion tends to be homogeneous, while at high temperatures, intergranular corrosion is preferred. The main depleted element due to Te interaction is chromium, as chromium tellurides exhibit the highest stability among the constituent elements.

In [13], the interaction between a 25% Ni, Nb stainless steel and Te vapour was analyzed. The reaction began above 450 °C, with a rate dependent on temperature. The corrosion occurred in three stages, ultimately forming a growing chromium telluride scale. Prolonged exposure to Te vapour at 650 °C and above led to intergranular attack and significant chromium depletion in the underlying matrix. At elevated temperatures, the extent of reaction product formation and intergranular penetration was constrained only by the initial tellurium concentration.

In [14], it was shown that in pure Te, ODS ferritic steels exhibited two corrosion layers at high temperature: an outer layer rich in Te and an inner layer rich in both Te and Cr. A chromium depletion zone was observed at the reaction front at 973 K after 100 hours. When the available Te was depleted, the system began converting all tellurides into the most stable forms, primarily chromium tellurides. During this process, Te diffused to the grain boundaries, reacting with chromium from the matrix and leading to intergranular attack. The formation of the two layers and the intergranular penetration is shown in Figure 2.3.

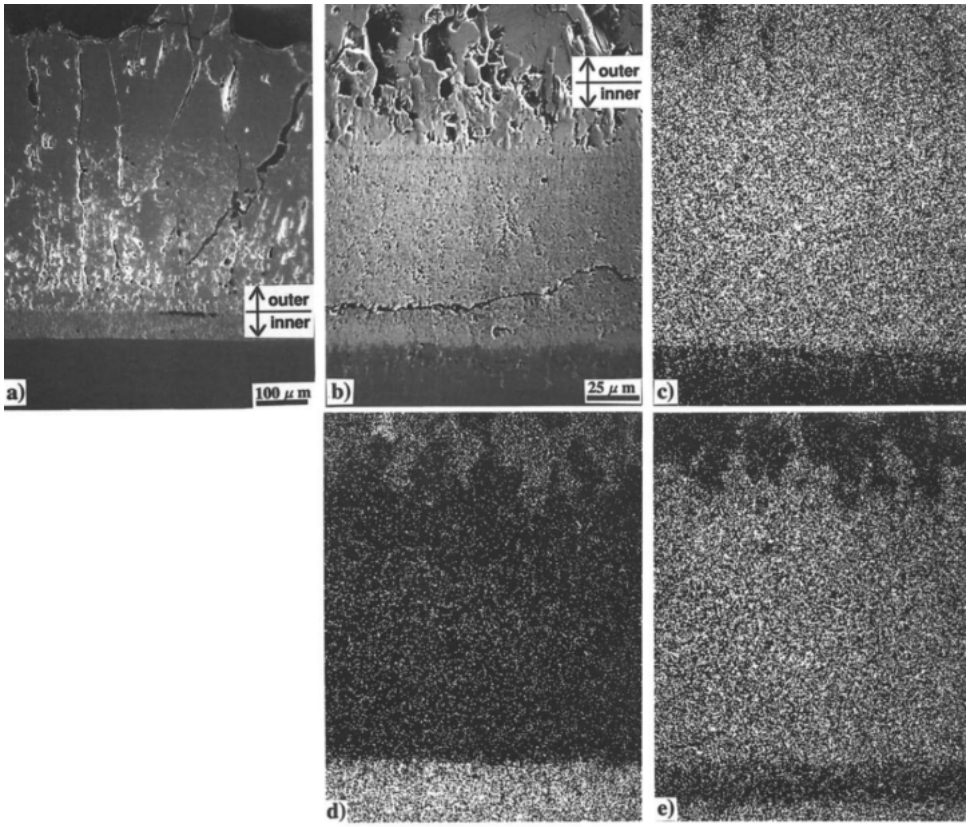

Figure 2.3: Cross section of austenitic PNC 316 stainless steel and ferritic ODS 130 cladding specimens after reaction with liquid Te at 973 K. a) PNC316 SEM image after 10 h exposure, b) ODS 13Cr SEM image after 100 h exposure, c) Te EPMA image for area b), d) Fe EPMA image for area b), e) Cr EPMA image for area b) [14].

2.5 Solute control

In a controlled environment formed by a liquid phase and a gas phase, solute concentration as oxygen in the liquid phase, can be retrieved from the partial pressure of the solute itself in the gas phase. This process requires knowledge of the relation between the solute partial pressure in the gas phase and the solute concentration in the liquid phase or metal alloy. The theory is the same used in other research as [22] and [23], explained in detail in [35]. This section presents fundamental concepts of physical chemistry, concluding with a brief explanation of how they are applied to ensure solute control.

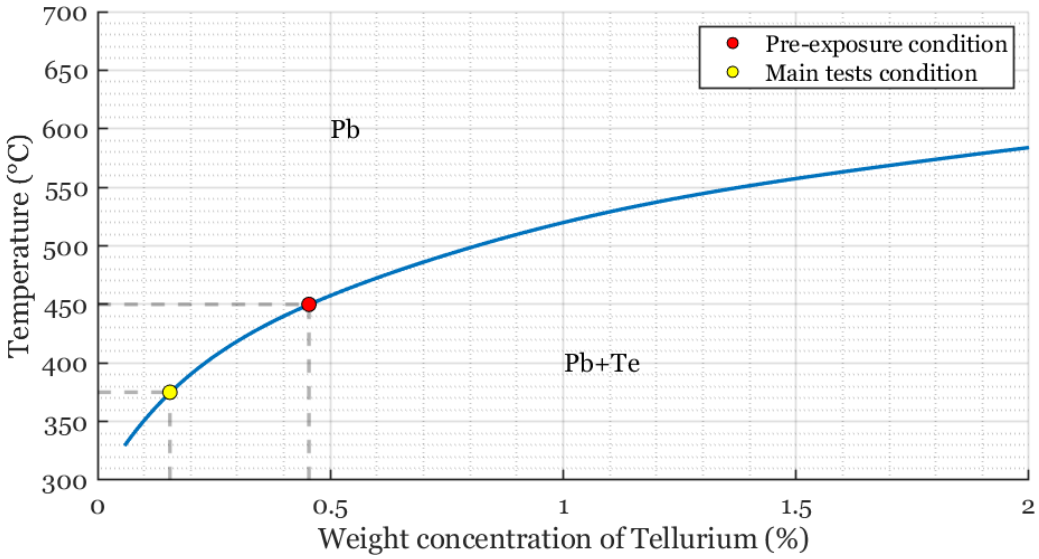

Figure 2.4: Pb-Rich Region of the Pb-Te Phase Diagram [34].

A metal oxidation can be represented by the following reaction:

$$xM + \frac{y}{2}O_2 \leftrightarrow M_xO_y$$

where M and O denote the metal and oxygen species, respectively. The tendency for oxide formation depends on both the temperature and the activity of oxygen. From the previous expression, it is evident that the oxide can revert to metal depending on these two factors (temperature and oxygen concentration). The Gibbs free energy for a system at constant temperature and pressure is given by:

$$G = H - T \cdot S$$

where G is the Gibbs free energy, H is the enthalpy, T is the temperature, and S is the entropy. For a reaction to occur spontaneously, the Gibbs free energy must be less than zero. By utilizing this relationship, the oxygen activity a_O required for the formation of the metal oxide M_xO_y can be determined.

Considering a generic reaction where reactants turn into products, the non-standard change in free energy ΔG is the instantaneous difference in free energy between reactants and products. This value is equal to:

$$\Delta G = \Delta G^\circ + RT \ln Q$$

The first value refers to the difference in free energy between reactants and products in their standard states at a specified temperature, R is the ideal gas constant, T is the absolute temperature in Kelvin, and Q is the reaction quotient. At equilibrium, the instantaneous difference in free energy between reactants and products is zero, which means there's no more driving force for the reaction. By definition, at equilibrium, the reaction quotient Q is equal to the equilibrium constant K. The upper equation becomes:

$$\Delta G^\circ = -RT \ln K$$

When it comes to formation of compunds from pure elements a f pedice is considered in the equation, and all the quantities mentioned beffore include la dicitura "of formation". Then, ΔG_f° is the standard gibbs free energy change of formation, and it is computed at different temperatures thanks to tabulated coefficents.

2.5.1 Activity

In thermodynamics, activity is the the measure of "effective concentration". It is useful to think of the activity for real mixtures as the concentration for ideal mixtures; chemical potential of a species in a mixture depends on its concentration in an ideal case, while depends on activity in a real case.

In other words, the activity is the concentration of solute in real condition that would be needed to exert the same vapor pressure if the solution possessed the properties of an ideal dilute solution. By definition, the activity of pure substances in condensed phases (solids and liquids) is taken equal to unity.

When it comes to non ionic solutions, it is possible to express the activity as:

$$a_{c,i} = \gamma_{c,i}\, c_i$$

Let's consider the general reaction:

$$\alpha A + \beta B \rightleftharpoons \rho R + \sigma S$$

Using activities, the equilibrium constant K for real (non-ideal) solutions can be expressed as:

$$K = \frac{a_R^\rho \, a_S^\sigma}{a_A^\alpha \, a_B^\beta}$$

In a metal oxidation reaction, considering the activities equal to one for the solid oxide and the liquid/solid metal, and the relationship between the activity of a gas and its partial pressure in a gas mixture as function of the oxygen partial pressure:

$$\Delta G^{\circ} = -RT \ln K(p_{O_2})$$

So, once the partial pressure of oxygen in the gas phase and the temperature are known, it is possible to retrieve the variation of Gibbs free energy for the oxidation of a metal.

2.5.2 Oxygen Concentration in Liquid Phase

In the frame of a liquid metal case. considering the oxidation reaction and the H_2O dissociation, computing ΔG° and considering the relationship between the activity of a gas and its partial pressure in a gas mixture, it is possible to retrieve the final formula that links the partial oxygen pressure at the outlet with the oxygen concentration in the liquid phase:

$$\frac{c_0}{c_{0,s}} = \frac{p_{\mathrm{H_2O}}}{p_{\mathrm{H_2}}} \frac{1}{\sqrt{p_{\mathrm{O_{2,s}}}}} \exp\left(\frac{\Delta_f G^{\circ}_{\mathrm{H_2O}}}{RT}\right)$$

where:

- c_0: is the desired value,
- $c_{0,s}$: is the oxygen concentration in the metal at saturation, can be computed thanks from numerous measurements,
- $\frac{p_{\mathrm{H_2O}}}{p_{\mathrm{H_2}}}$: is measured by the sensor,
- $\Delta_f G^0_{\mathrm{H_2O}}$: is computed thanks to tabulated coefficients with respect to temperature,
- $p_{\mathrm{O_{2,s}}}$: this value is obtained from the oxide that is either desired or undesired for formation. In the case where the metal can no longer accommodate diluted oxygen, oxidation and precipitation will occur. Thus, the oxygen partial pressure at saturation will be the value derived from the equation for the change of Gibbs free energy in the formation reaction of that specific oxide.

2.6 Related Work

Studies have recorded LME in molten Pb for ferritic steels such as [36]. This study investigated the behavior of a ferritic-martensitic steel in a pure molten lead environment. In this study, despite the surface treatment applied before testing to facilitate contact between the liquid metal and the steel, it was not possible to completely prevent the formation of a protective oxide layer.

Unnotched specimens exhibited no evidence of LME across the entire temperature range considered (350–450°C). At 350°C, oxide formation was minimal, making a detailed investigation challenging. This can be attributed to the lower oxygen concentration at lower temperatures, as well as the reduced oxidation kinetics. In contrast, at 450°C, the presence of a well-developed oxide layer was clearly observed. Although minimal, this oxide layer remained sufficiently intact under loading conditions, preventing the propagation of a brittle fracture due to LME.

For notched specimens, LME was detected. It is hypothesized that this occurred because the notch acted as a stress concentrator, generating sufficiently high local stresses to damage the protective oxide layer. This disruption allowed direct contact between lead and steel, ultimately leading to embrittlement.

In both cases, conclusions were supported by fractographic analysis. In summary, the T91 steel examined in this study is chemically susceptible to LME. However, as dictated by the fundamental condition for LME, embrittlement occurs only when direct contact between Pb and steel is ensured—meaning that the oxide layer must either be absent or compromised.

2.7 Basis for the Present Work

This study builds upon the work presented in [23], utilizing the same experimental setup and methodologies while expanding the investigation to assess the effects of tellurium in liquid lead. Although the focus of this research is on the influence of tellurium, it is crucial to first summarize the findings obtained in the previous study, which analyzed the behavior of 10-4 steel in pure liquid lead.

The results from [23] demonstrated that unnotched specimens exhibited no evidence of LME throughout the entire temperature range considered (340–480°C). This was

observed despite ensuring good wettability between the liquid lead and the steel surface, suggesting that 10-4 is inherently resistant to LME in pure lead environments. However, a more probable explanation is the presence of a protective oxide layer, which naturally forms on the steel surface and prevents direct contact between the liquid metal and the underlying material. This oxide layer appears to be difficult to avoid under the experimental conditions used.

The absence of LME in pure lead is a significant finding, as it indicates that 10-4 steel could be a promising candidate for structural applications in lead-cooled nuclear systems.

Chapter 3

Materials and Methods

3.1 Materials

3.1.1 Lead

The lead used for the experimental campaign was sourced from Aldrich Chemistry (product code 296177-2KG). The material consists of lead shot with a maximum diameter of less than 2 mm and a purity of 99.9% on a trace metal basis. This high-purity lead was selected to minimize the presence of contaminant elements that could interfere with the results, particularly in corrosion and embrittlement studies. The physical form of the lead (small spherical shots) allowed for an efficient melting procedure.

3.1.2 Tellurium

The tellurium used in the tests was supplied by Thermo Scientific (product number 315991000). The material is in powdered form with a mesh size of 200 and a purity of 99.8% on a trace metal basis, ensuring suitability for sensitive metallurgical experiments.

3.1.3 FeCrAl

The main material analyzed in this study is a Fe10Cr4Al alloy, developed by Alleima, supplied by Kanthal (owned by Alleima); this same alloy was employed in [23], making it suitable for direct comparison with the referenced study. This steel incorporates

Reactive Elements (RE), which enhance both its corrosion resistance and mechanical performance [37]. The detailed chemical composition is provided in Table 3.1. The samples, supplied by Kanthal, were subjected to hot rolling and annealing at 1050°C for 45 minutes.

3.1.4 Stainless Steel 316L

AISI 316L stainless steel was used as a reference material for comparison, since it has always been a candidate as a cladding material. Its composition is shown in Table 3.1.

Table 3.1: Chemical composition of 10–4 and 316L alloys in wt%.

Alloy	Ni	Al	Cr	Mo	Si	Mn	C	RE
10–4	–	4.0	10.0	–	0.15	–	<0.05	Ti, Nb, Zr
316L	10.1	–	16.9	2.0	0.52	0.95	0.02	–

3.2 Slow Strain Rate Testing Rig

The rig allows tensile tests while the specimen is held in a controlled atmosphere. In particular, the specimen is placed inside a chamber where the inlet purge gas and outlet oxygen content are monitored to ensure the desired oxygen concentration in the molten metal. The chamber can be partially filled with molten metal thanks to an external heater. All components not in direct contact with the molten metal are made of 316L, while those in contact are manufactured from 10-4, as this alloy has demonstrated high corrosion resistance [37]. The data are then transmitted to an external computer. The scheme of the rig is shown in Figure 3.1

All the samples were manufactured to fit the specification shown in Figure 3.2.

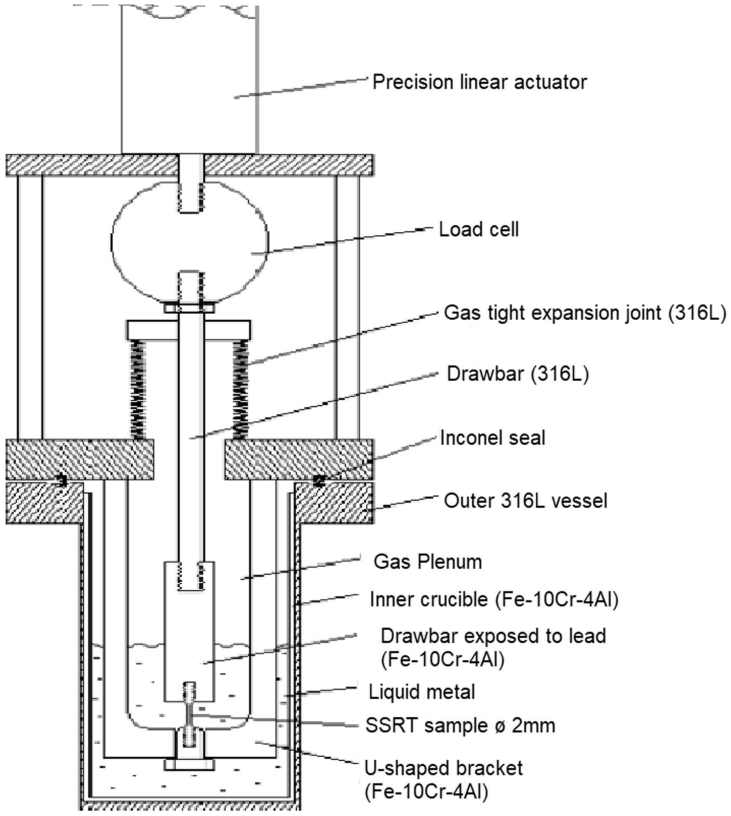

Figure 3.1: Scheme of the SSRT rig [23]. The figure shows, at the bottom, the chamber where the specimen is immersed in the molten metal and subjected to tensile loading. At the top are the traction system, the hermetic sealing for the controlled atmosphere, and the load cell, which records and outputs the force signal.

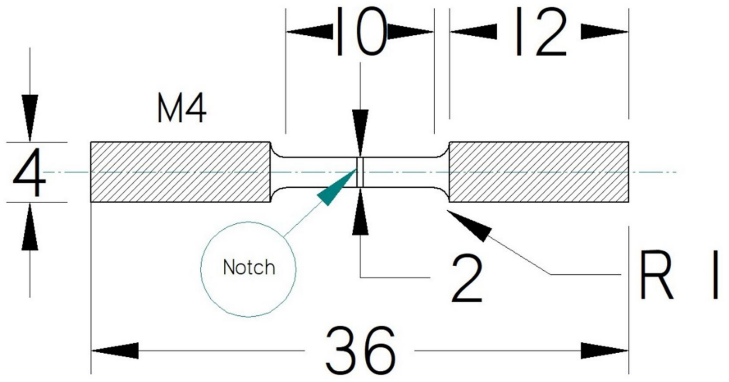

Figure 3.2: Specifications of the SSRT sample, given in mm varies by ±0.1 mm [23]. Part of the specimens used do not feature the central notch.

3.3 Methodologies and Experimental Parameters

In the following section, the general procedure regarding the test is explained, then every intermediate stage and aspect is more deeply described. Finally, all the tests performed following the previous procedure are presented.

3.3.1 Experimental Procedure

The rig purpose is to test stress-strain specimens in a controlled environment, specifically controlling molten metal temperature and oxygen concentration within. When the test involved a molten metal enviroment, the specimen was pre-exposed to oxygen-free molten metal at 450 °C for the range of 22-24 h to enhance surface wettability and establish close metal-to-specimen surface contacts, as done in [23][38]. Following the pre-exposure process, the temperature was then switched to the target tensile testing temperature. The oxygen concentration in dissolved molten metal was reduced flushing Ar $+$ 5% H_2 gas from the inlet pipe into the atmosphere right above the molten metal. The equilibrium between the gas phase and the liquid phase of the chamber ensure the oxygen concentration control in the metal. After the test, the two broken specimen parts were removed and cleaned using a solution composed of acetic acid ($C_2H_4O_2$), hydrogen peroxide (H_2O_2), and deionized water in a 1:1:1 ratio. The samples were submerged in this solution for 45 minutes to 1 hour. Afterwards, they were rinsed with deionized water and dried with paper.

3.3.2 Experimental Parameters and Variable Control

The tests involved temperature ranging from room temperature to 550°C. The enviroments were ArH_2 atmosphere condition, pure lead and lead doped with changing tellurium concentration. The wanted weight-concentration of the tellurium in the mixture has been accomplished first by adding solid tellurium to the molten lead. Later, the process has been modified, adding the solid tellurium after the molten lead has cooled down to solid form. This because of the thermal shock between the room-temperature tellurium and the molten lead causing their contact to result in an exotermic reaction that caused a partial loss of the tellurium and a deviation in the wanted concentration of the tellurium.

The low oxygen environment was achieved by flushing the system with a gas mixture of Ar $+ 5\%$ H_2, the outled of the chamber is then routed through a Zirox SGM5 oxygen analyzer; here the gas is heated to 750°C, and the resulting electrical potential in the yttria-stabilized zirconia (YSZ) oxygen probe is measured to determine the oxygen concentration [39]. It is calibrated by "ZIROX – sensoren und Elektronik GmbH," Germany. Pre-exposure was done by flushing the system using the same gas to decrease oxygen partial pressure and to allow it to equilibrate at a pressure less than $C_O < 10 - 10wt\%$, see Figure 2.1, dissolved oxygen in the liquid metal. The oxygen levels of the SSRT equilibrated after a time of 3 hours. The variations of the oxygen levels during actual SSRT run were negligible. The crosshead speed, i.e., the speed at which the testing machine's drawbar travels during the test, can be set using the rig's software.

The values shown in the graphs within the chapter 4 are expressed in terms of engineering stress and strain, meaning that the reduction of the cross-sectional area during deformation has not been taken into account. Engineering strain refers to the amount of deformation in the direction of the applied load, divided by the original gauge length of the specimen. Only the permanent elongation (plastic deformation) is considered. This quantity can also be expressed as the fracture elongation A, i.e., the relative displacement between two reference points after fracture, expressed as a percentage. The engineering strain is calculated as:

$$\varepsilon = \frac{\Delta L}{L_0}$$

where ΔL is the change in length and L_0 is the initial length of the specimen. Engineering stress is defined as the applied force F divided by the original cross-sectional area A_0 of the specimen:

$$\sigma = \frac{F}{A_0}$$

3.3.3 Overview of Performed Tests and Rationale

The red regions in Figure 2.1 indicates the oxygen concentrations for the experiments. These concentrations enable the growth of Fe_3O_4 at reduced temperatures but also support the formation of $FeAl_2O_4$, $FeCr_2O_4$, Cr_2O_4, and Al_2O_3 on the steel specimens. These oxide formation lines occur at an even lower ΔG than those depicted in Figure 2.1. In Figure 3.3 the tests oxygen condition is shown compared to the reference temperature of the test itself.

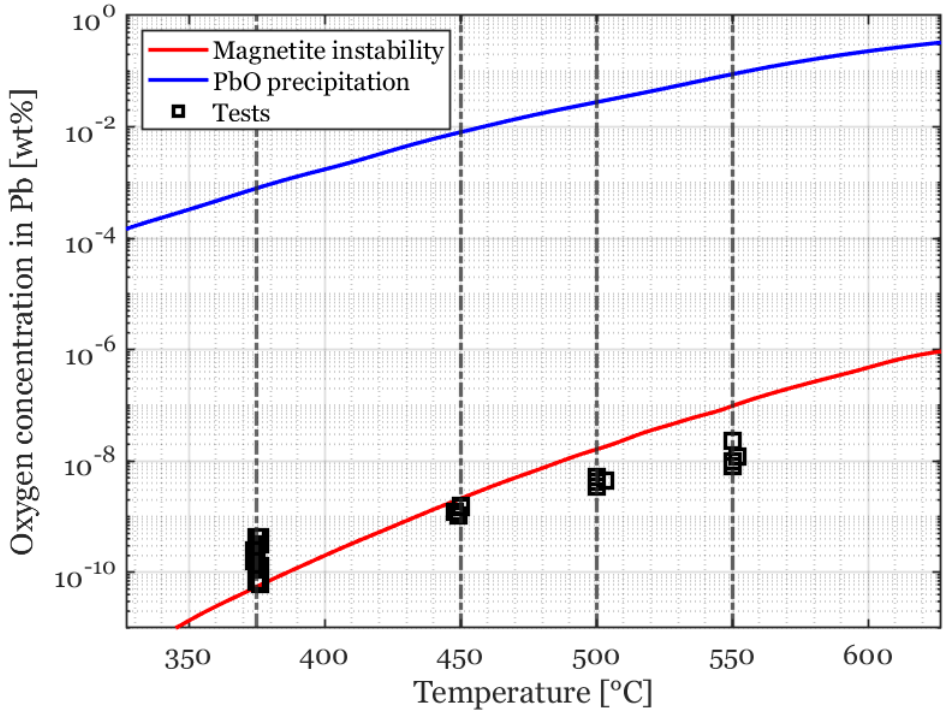

Figure 3.3: The graph plots oxygen concentration in lead (logarithmic scale) against temperature. It shows stability lines for lead oxyde and iron magnetite oxyde. Experimental conditions are represented, they are located between these lines, tracking closer to the ”Magnetite instability” line [40].

The first batch of tests involved unnotched specimens, so the following discussion will refer to them. Reference tests with 10-4 and 316L were carried out in a pure ArH_2 atmosphere at ambient temperature and at 375 °C, which is the experimental target temperature since it is near the melting point of lead and hence in the range where LME would become more prominent. Then, 10-4 and 316L steels were tested in pure liquid lead at 375 °C, 450 °C, 500 °C, and 550 °C as reference tests. Subsequently, 10-4 specimens were tested in environments with increasing tellurium concentration, gradually up to an amount of 1.2 wt%. Precipitation around the specimen and

apparatus showed that the solubility point of tellurium in lead had been reached, as indicated in the referenced Figure 2.4. For this purpose, further tests were performed maintaining the 1.2 wt% concentration but raising the temperature to 550 °C for both 10-4 and 316L. The concentration of tellurium was not increased further since, even in the worst possible scenarios, the highest expected value is roughly an order of magnitude lower; furthermore, dissolving higher percentages of tellurium would require higher temperatures, thus reducing the potential for LME and introducing other kinds of issues. Tests at 375 °C in pure lead and in lead with variable tellurium concentration were also carried out by changing the crosshead speed. The latter was decreased to observe any effects that the crack opening speed may have on the interaction between the two phases and on the fracture mode. Although the tensile testing machine is consistently set to predefined crosshead speeds (e.g., 2×10^{-3} mm/s and 1×10^{-4} mm/s), the actual strain rate may slightly differ from one test to another. This is due to minor variations in the displacement control system and transient mechanical responses, which introduce small inconsistencies in the applied speed. Therefore, the strain rate is calculated individually for each test based on the actual displacement data. On average, the nominal speeds correspond to strain rates of approximately $R_1 = 5.6 \times 10^{-5}\,\mathrm{s}^{-1}$ and $R_2 = 2.86 \times 10^{-6}\,\mathrm{s}^{-1}$, respectively.

The second batch of tests was carried out with 10-4 specimens featuring a notch in the middle, to examine the effect of stress concentration on the LME phenomenon. Initial reference tests were conducted in an ArH_2 atmosphere at both room temperature and 375 °C. These were followed by reference tests in pure molten lead at 375 °C. Subsequently, tests were performed in molten lead environments doped with varying concentrations of tellurium. It is important to note that all notched specimens were tested using the strain rate R1.

A complete overview of all the performed tests, including specifications, is provided in Table 3.2.

3.4 Analysis and Characterization

Following cleaning, the samples were characterized and analyzed using a Hitachi S-3700N SEM equipped with an Energy Dispersive Spectroscopy (EDS) system for elemental analysis.

Table 3.2: Comprehensive list of all tests performed, including experimental conditions. The columns include the test identification code, the presence or absence of a notch, the test environment conditions (i.e., presence or absence of lead and tellurium), the reference test temperature, and finally the strain rate used.

Code	Steel	Notch	Pb	Te [wt%]	Temp. [°C]	Strain Rate
1	10-4	no	no	0	23	R1
2			no	0	23	
3			no	0	375	
4			no	0	375	
5			yes	0	375	
6			yes	0	375	
7			yes	0.01	375	
8			yes	0.01	375	
9			yes	0.1	375	
10			yes	0.1	375	
11			yes	0.2	375	
12			yes	0.2	375	
13			yes	0.3	375	
43			yes	0.3	375	
14			yes	0.6	375	
15			yes	0.8	375	
16			yes	1.2	375	
50			yes	1.2	375	
24	316L	no	no	0	24	R1
23			no	0	375	
29			no	0	450	
52			no	0	450	
30			no	0	500	
31			no	0	550	
28			yes	1.2	375	
22			yes	1.2	450	
21			yes	1.2	500	
20			yes	1.2	550	
25	10-4	no	no	0	450	R1
26			no	0	500	
27			no	0	550	
19			yes	1.2	450	
18			yes	1.2	500	
17			yes	1.2	550	
37	10-4	no	yes	0	375	R2
45			yes	0.6	375	
47			yes	1.2	375	
32	10-4	yes	no	0	26	R1
33			no	0	26	
34			no	0	375	
35			no	0	375	
36			yes	0	375	
38			yes	0.01	375	
39			yes	0.01	375	
40			yes	0.1	375	
41			yes	0.1	375	
42			yes	0.3	375	
44			yes	0.6	375	
46			yes	0.8	375	
48			yes	1.2	375	
49			yes	1.2	375	

Chapter 4

Results

4.1 Unnotched Samples

4.1.1 316L Samples

Here, 316L tests in pure ArH_2 atmosphere at increasing temperatures are presented. The stress-strain curves are shown in Figure 4.1. All curves at higher temperatures exhibit comparable fracture strains. A significant reduction in Ultimate Tensile Strength (UTS) and fracture strain compared to the room temperature test is observable.

316L steel has been tested in pure ArH_2 atmosphere and in lead with 1.2 wt% tellurium at 375°C, 450°C, 500°C and 550°C. The corresponding stress-strain curves are shown in Figure 4.2. Comparing each pair of graphs, no systematic behavior related to the presence of lead and tellurium is observed. Even when considering the temperature variation, no clear effect can be identified. In Figure 4.3, SEM images of some of the aforementioned specimens are presented. The images showing a specific area rather than the entire fracture surface were selected because they are representative of the overall fracture morphology. Overall, the behavior is ductile, and dimples of various shapes and sizes are clearly visible. No evidence of brittle fracture is observed.

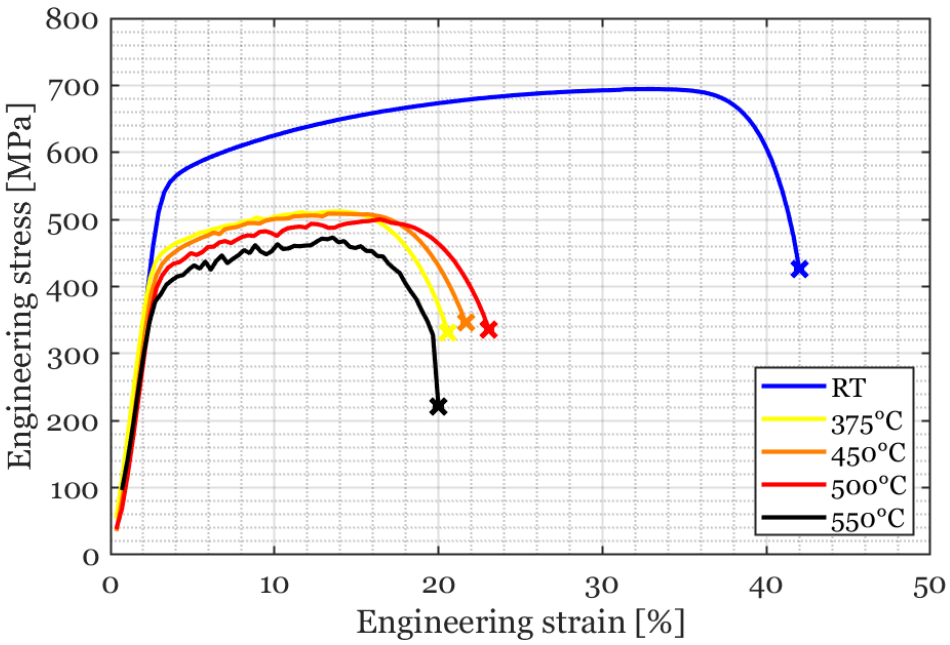

Figure 4.1: Stress-strain curves of reference 316L specimens in pure Ar_2. R1 strain rate.

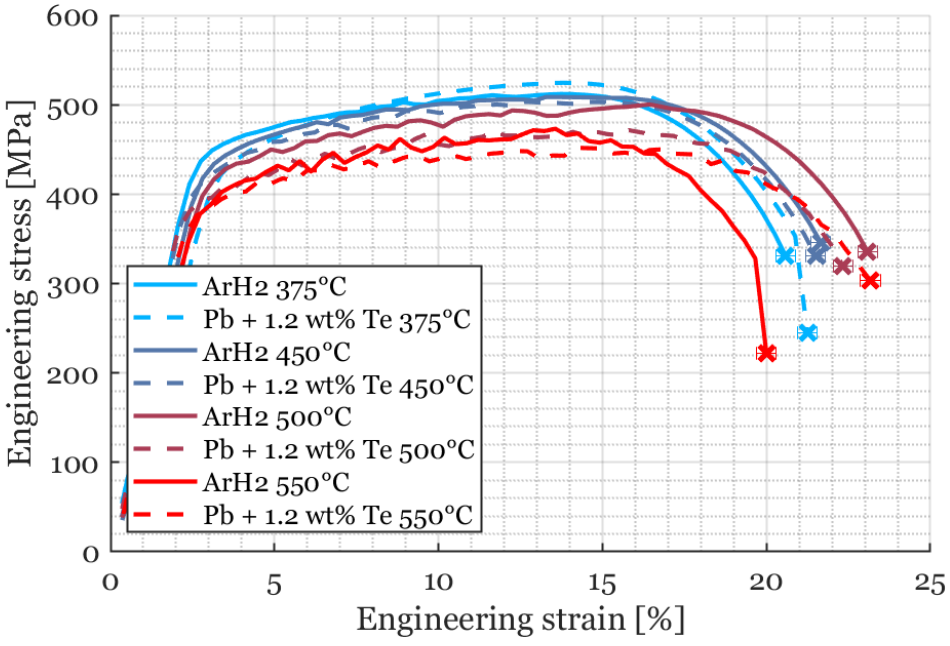

Figure 4.2: Engineering stress-strain curves of 316L specimens tested at various temperatures in two environments: pure ArH_2 and Pb with 1.2 wt% Te. R1 strain rate. Each pair of curves at the same temperature allows a direct comparison of mechanical behavior under different environmental conditions.

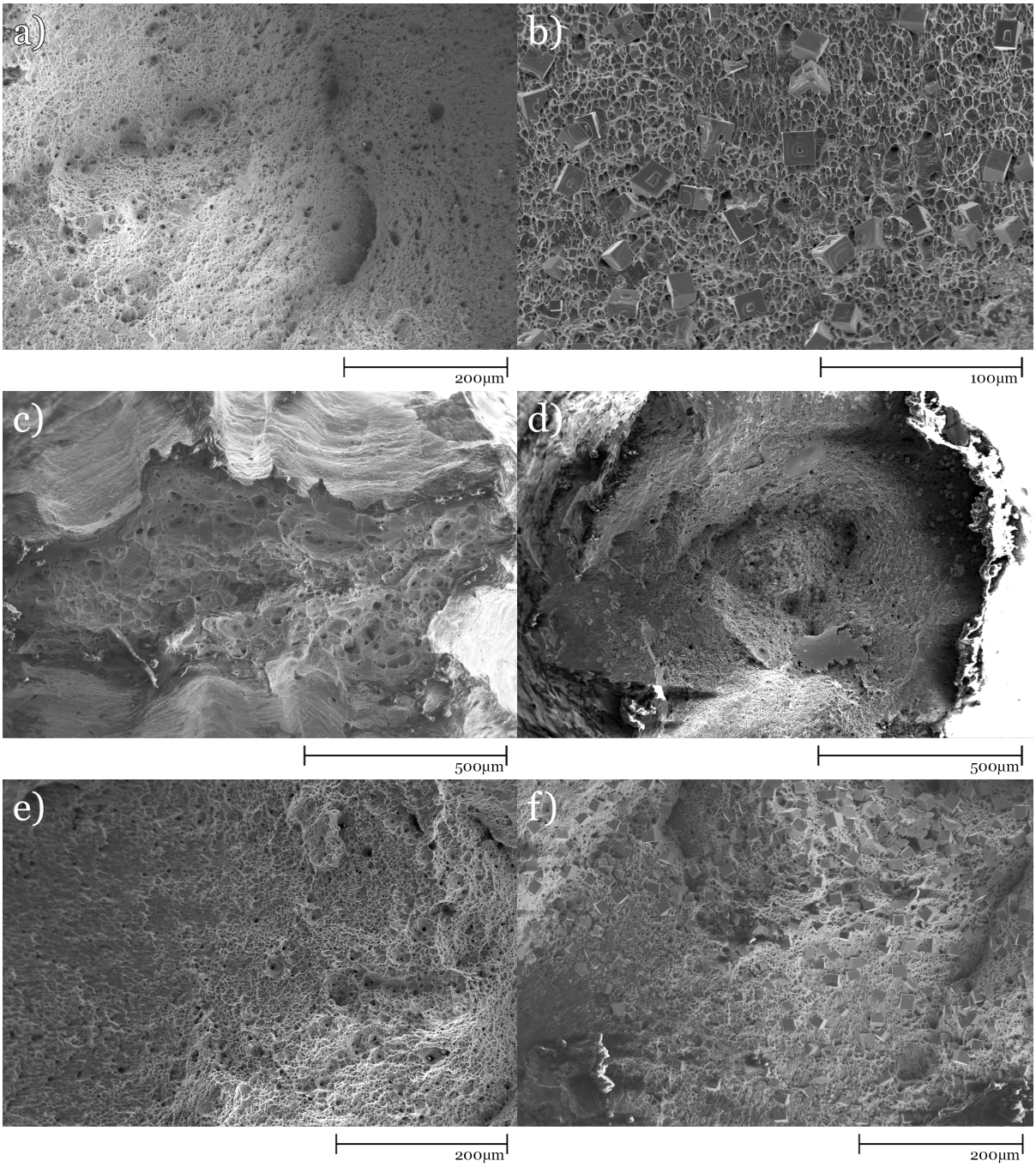

Figure 4.3: Fracture surfaces show necking formation in the different unnotched 316L samples a) ArH_2 450°C, b) Pb+1.2 wt% Te 450°C, c) ArH_2 500°C , d) Pb+1.2 wt% Te 500°C, e) ArH_2 550°C and f) Pb+1.2 wt% Te 550°C. R1 strain rate.

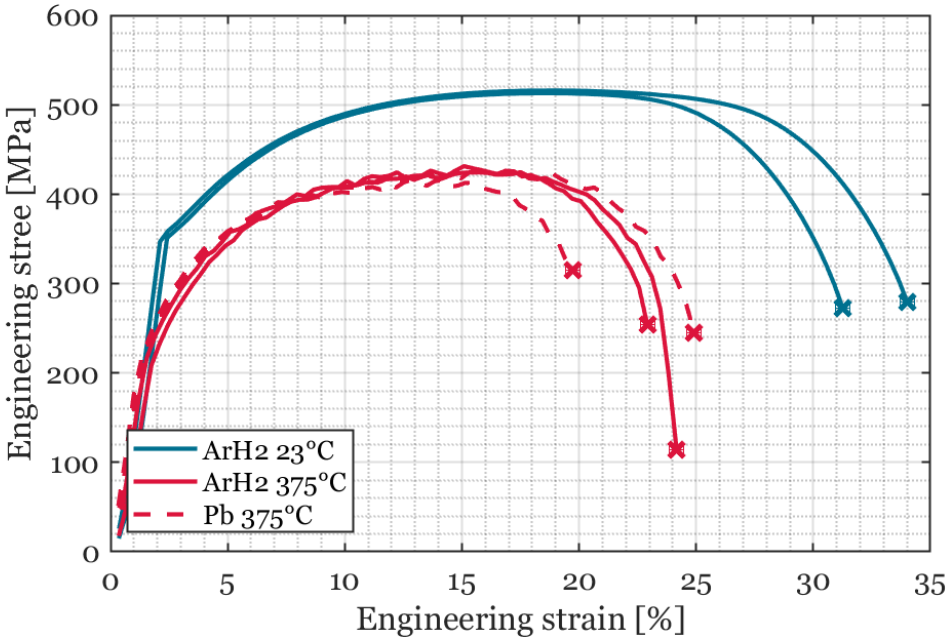

Figure 4.4: Stress-strain curves of reference unnotched 10-4 specimens in different enviroments. R1 strain rate.

4.1.2 10-4 Samples

Considering 10-4 tests in pure ArH_2 atmosphere and pure lead, stress-strain curves are shown in Figure 4.4. The curves of samples in ArH_2 atmosphere at 375°C show lower UTS and maximum elongation compared to the ones in same atmosphere but ambient temperature (26°C). The curves of the specimens in lead are comparable to the ones at same temperature in simple ArH_2 atmosphere.

The examination of fracture surfaces in specimens tested under an ArH_2 atmosphere revealed no significant changes in appearance with increasing test temperature. The fracture mode remained ductile across the entire surface, characterized by typical dimpled ductile fracture at the specimen's center, transitioning into shear fracture near the surface. This is still true when it comes to samples pulled at same temperature in pure lead. The SEM pictures of the fracture surface of the upper mentioned specimens are shown in Figure 4.5.

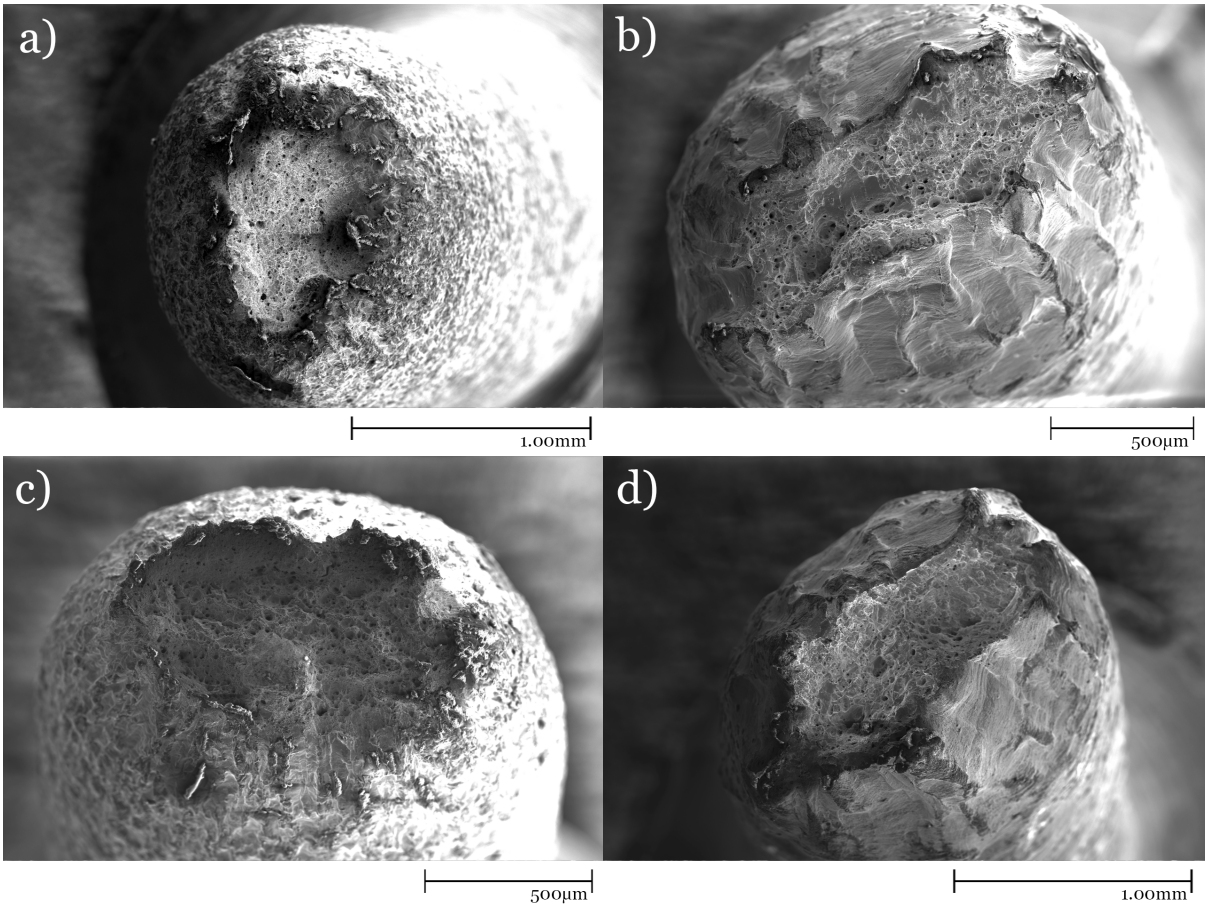

Figure 4.5: Fracture surfaces show necking formation in different unnotched 10-4 samples, R1 strain rate in: a) ArH_2 room temperature (23°C), b) ArH_2 atmosphere at 375°C, c) pure Pb at 375°C, and d) pure Pb at 375°C (replicate test).

Tests on 10-4 steel performed in pure lead are compared to those with increasing reference Te concentration; their stress-strain curves are shown in Figure 4.6. The red curves, representing the results for two specimens in pure lead, show how final total elongation varies by around 5% for the same test. The dark blue curves describe tests with increasing Te concentrations. Finally, the green curve refers to the test with the highest Te concentration used in this study; their total final elongation falls within the same range as the others while the UTS is higher compared to the rest. The total final elongations of tests in which the Te concentration in lead was increased do not show a clear underlying trend or phenomenon. This can be seen from Figure 4.7, where fracture strain is plotted with respect to reference Te concentration. From the curves, the total final elongation of tests in which the reference Te concentration in lead was increased does not show a clearly unfolding phenomenon related to the tellurium. However, Figure 4.7 suggests a trend with a minimum at 0.3 wt% Te, indicating that this concentration might have a bigger effect on ductility.

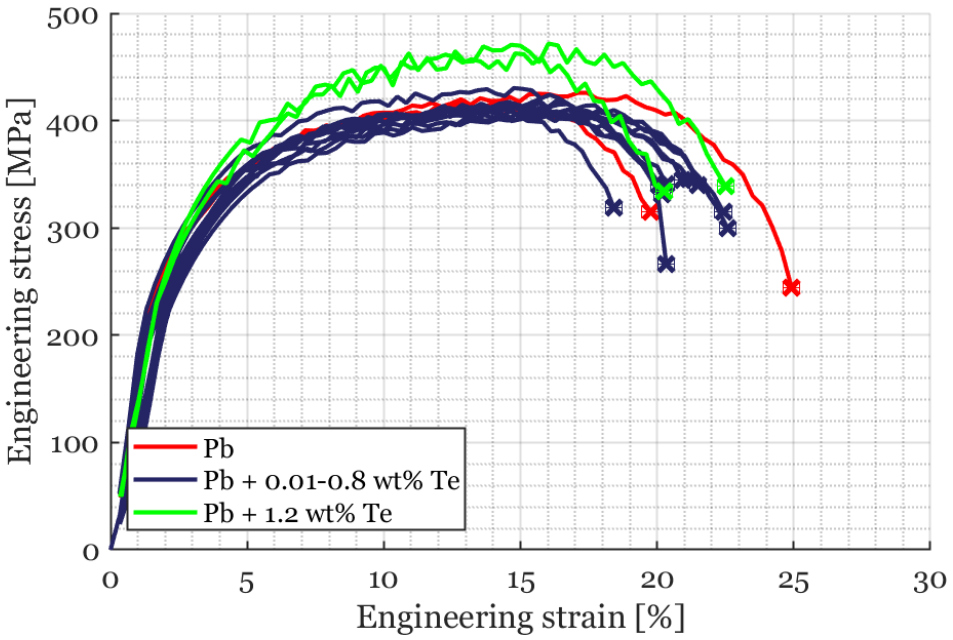

Figure 4.6: Stress-strain curves of unnotched 10-4 specimens tested at 375°C in pure lead and in lead with added tellurium. R1 strain rate.

In Figure 4.9, SEM pictures of some relevant specimens from Figure 4.6 are shown. As observed previously, the test on pure lead exhibits clear dimples and a ductile fracture. With the smallest tellurium concentration used in these tests (i.e., 0.01 wt%), the fracture surface already shows a cleavage-like appearance. This trend persists as the concentration increases to 0.1 wt%, 0.3 wt%, and 0.6 wt%. Finally, at 1.2 wt%, the fracture surface returns to being mainly characterized by dimples, with some traces of brittle fracture behavior still observable in both specimens tested under those conditions.

For different temperatures, 10-4 tests in pure ArH_2 atmosphere are compared to those performed in lead with 1.2 wt% tellurium. The corresponding stress-strain curves are shown in Figure 4.8. By comparing each pair of tests, the effect of temperature is evident, with a reduction in both the UTS and the fracture strain as temperature increases. However, when comparing each test in pure ArH_2 with its counterpart in Pb + 1.2 wt% Te, no significant effect on ductility is observed.

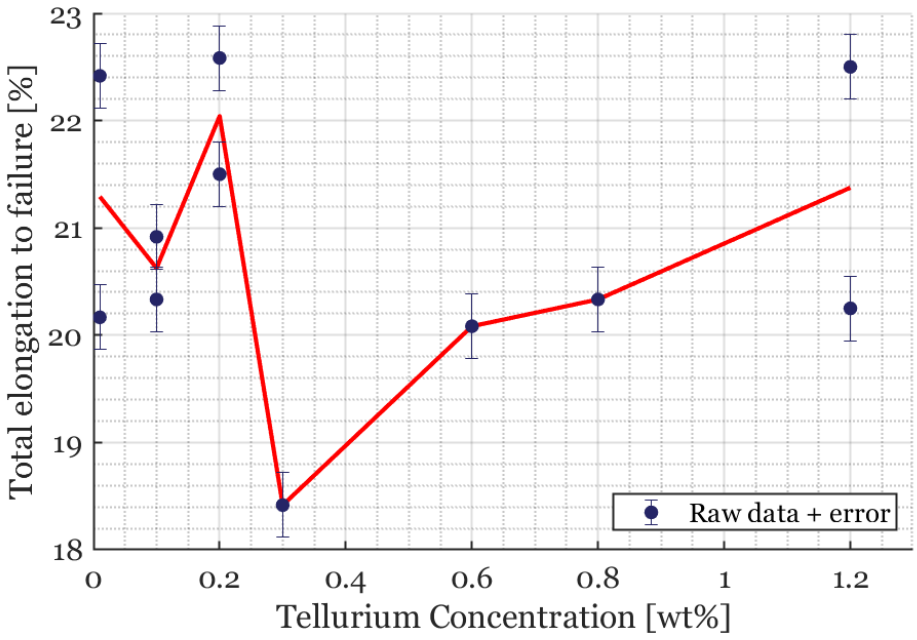

Figure 4.7: Total final elongation of unnotched 10-4 specimens tested in lead at 375°C with increasing tellurium concentration. R1 strain rate.

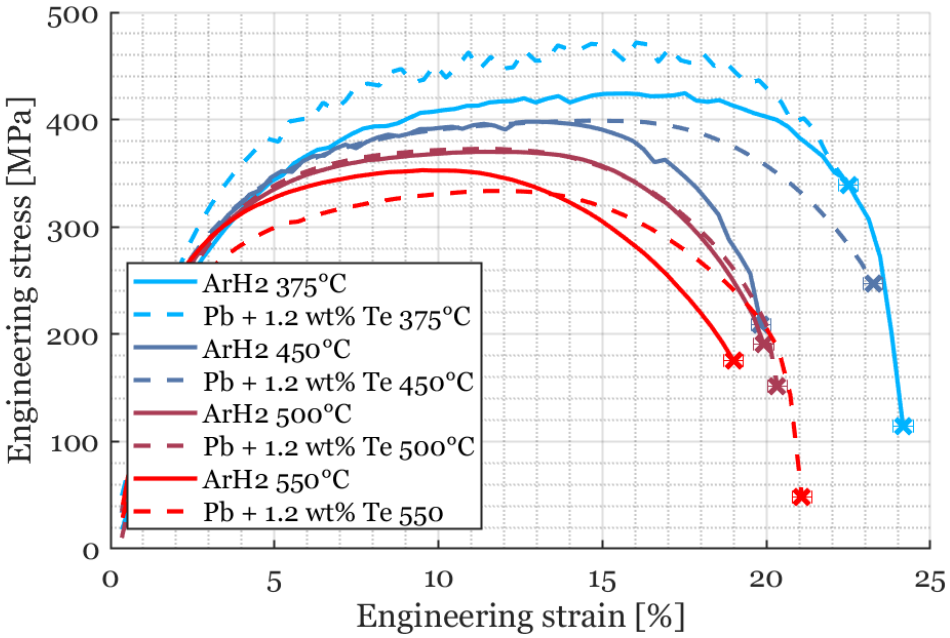

Figure 4.8: Engineering stress-strain curves of unnotched 10-4 specimens tested at various temperatures, R1 strain rate, in two environments: pure ArH_2 and Pb with 1.2 wt% Te. Each pair of curves at the same temperature allows a direct comparison of mechanical behavior under different environmental conditions.

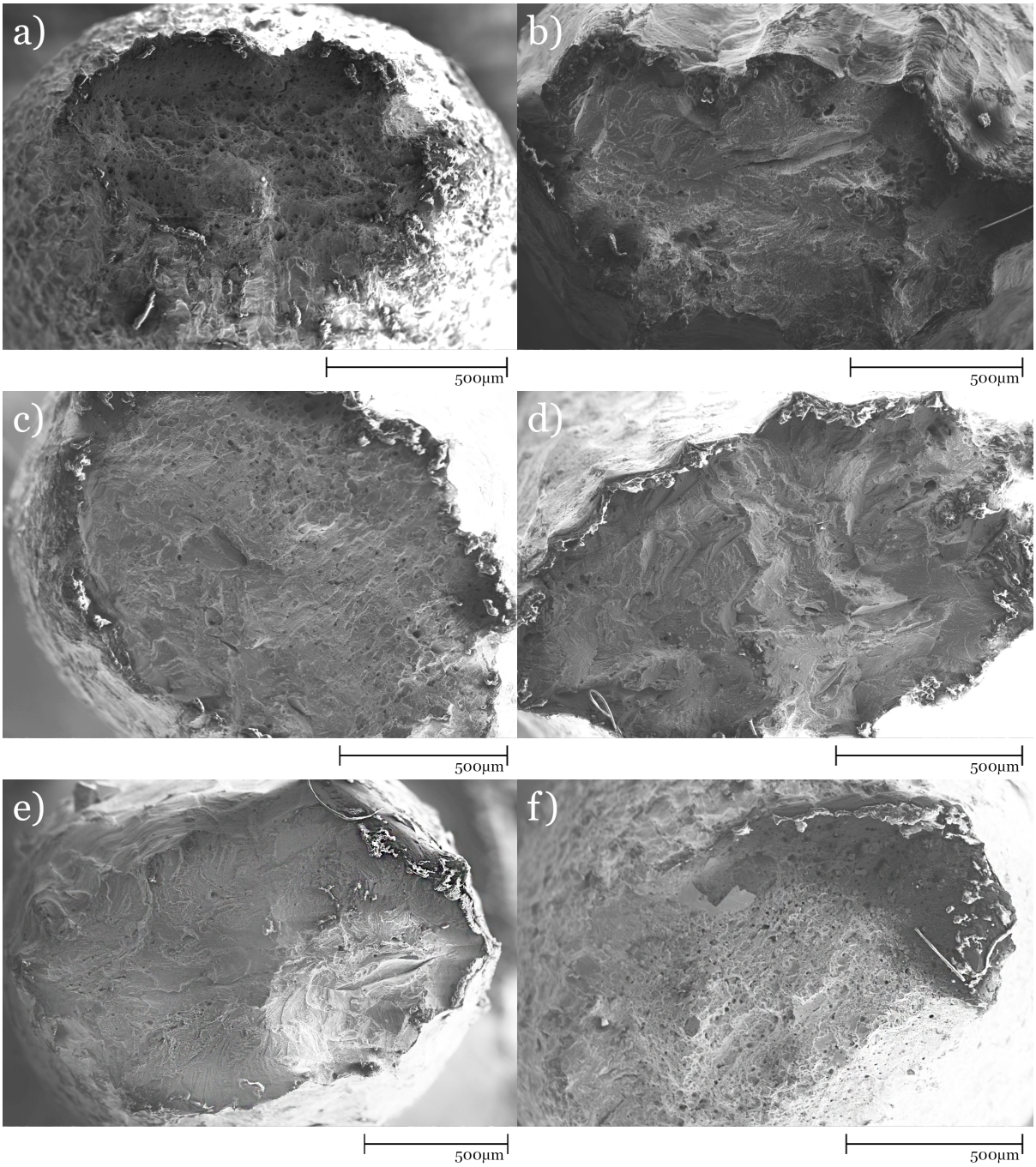

Figure 4.9: Fracture surfaces show necking formation in the different unnotched 10-4 samples, R1 strain rate tested in: a) pure Pb, b) Pb+0.01 wt% Te, c) Pb+0.1 wt% Te , d) Pb+0.3 wt% Te, e) Pb+0.6 wt% Te and f) Pb+1.2 wt% Te.

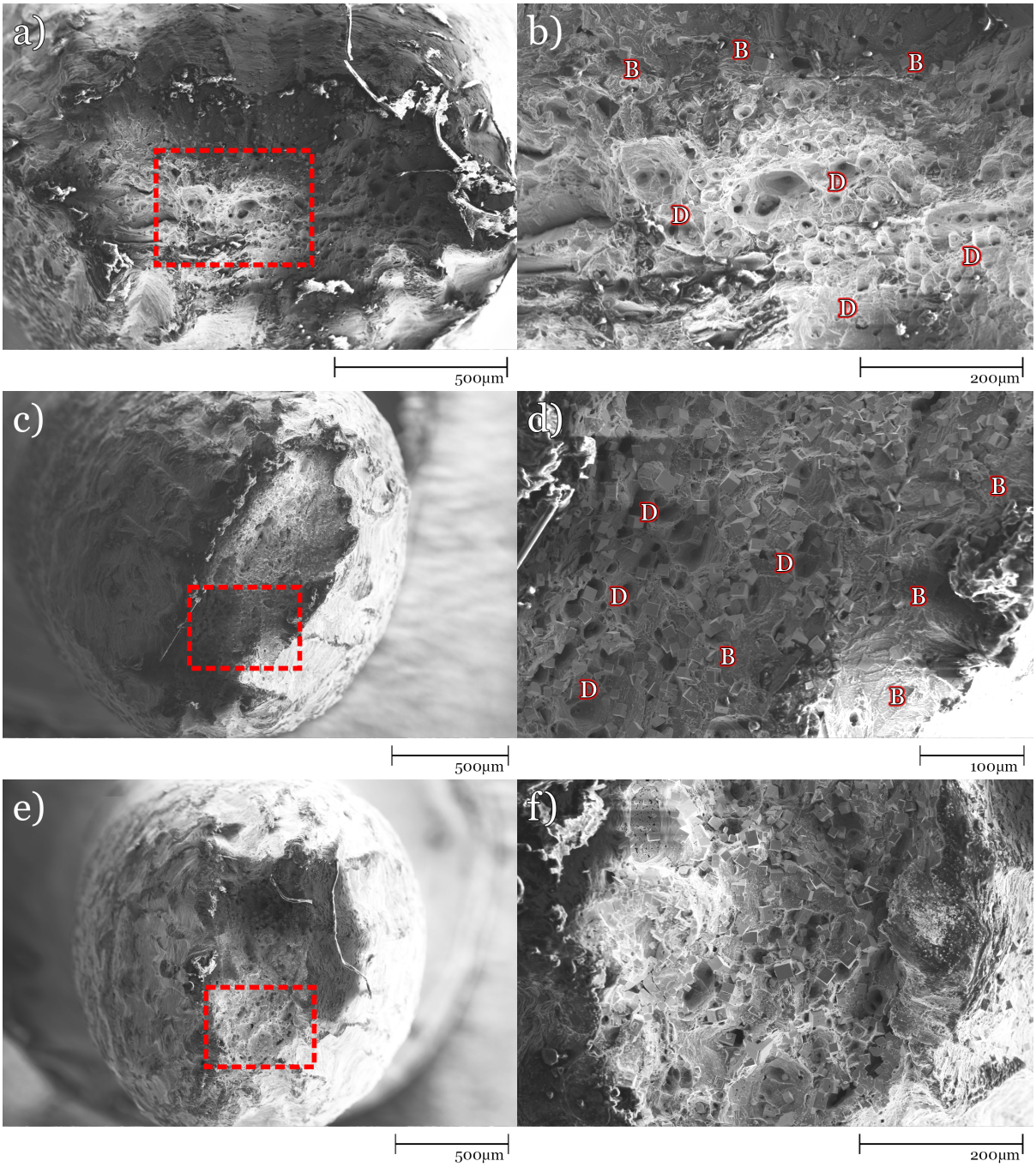

Figure 4.10: Fracture surfaces show necking formation in different unnotched 10-4 samples, R1 strain rate in: a) Pb+1.2 wt% Te 450°C, b) same as a) but zoomed on the red box, c) Pb+1.2 wt% Te 500°C , d) same as c) but zoomed on the red box, e) Pb+1.2 wt% Te 500°C and f) same as e) but zoomed on the red box. Letters ”B” and ”D” respectively mean ”brittle” and ”ductile” fracture appearance.

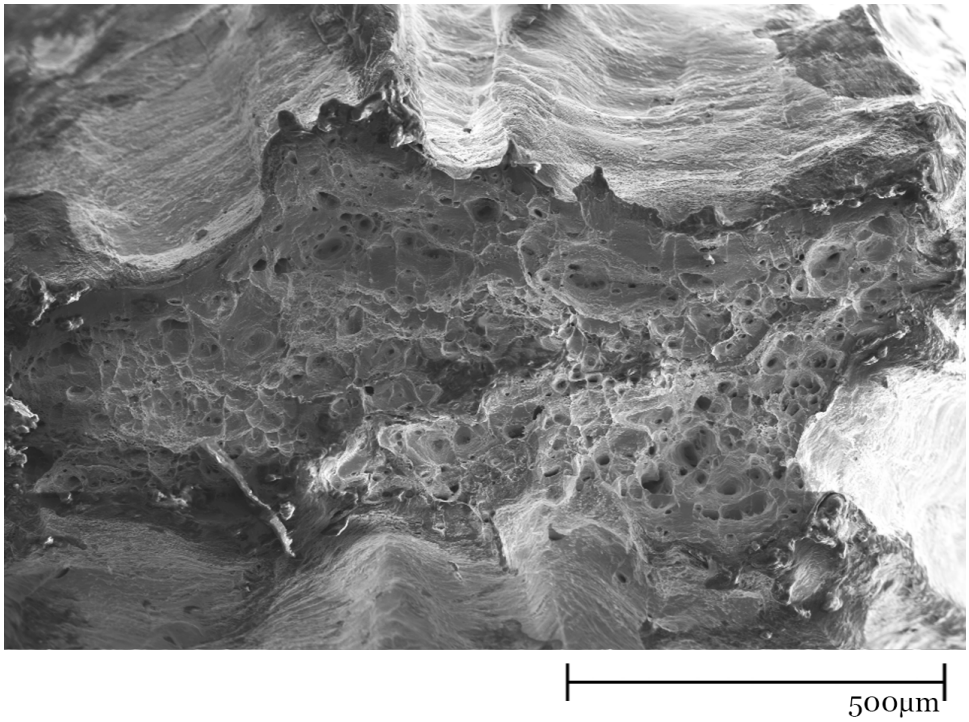

Figure 4.11: SEM picture of fracture surface of unnotched 10-4 specimen in ArH_2 at 500°C. R1 strain rate.

In Figure 4.10 some SEM images from 10-4 specimens tested at different temperature in Pb+1.2wt% Te are shown. These fracture surfaces do not show any variation in the fracture mode, which remains entirely ductile. However, regions where the fracture appears brittle are visible in the Pb+Te samples within the intermediate temperature range (450°C / 500°C). The corresponding specimens tested in ArH_2 all exhibit a clearly ductile fracture, with no signs of brittle fracture. Figure 4.11 provides a reference showing how all the surfaces appear.

Tests on 10-4 steel performed in pure lead are compared to those carried out with increasing reference Te concentrations. The strain rate was kept constant at R2, and the corresponding stress-strain curves are shown in Figure 4.12. The three curves, red for pure lead, blue with 0.6 wt% Te, and green for 1.2 wt% Te, exhibit a similar fracture strain, indicating that tellurium does not have a significant effect at these concentrations. However, the curve corresponding to 0.6 wt% Te shows a considerably lower UTS. In Figure 4.13, the fracture surfaces of the aforementioned specimens are shown. The presence of dimples and necking is clearly visible, indicating a fully ductile fracture. In the specimen with 0.6 wt% Te, some small features may be associated with brittle fracture.

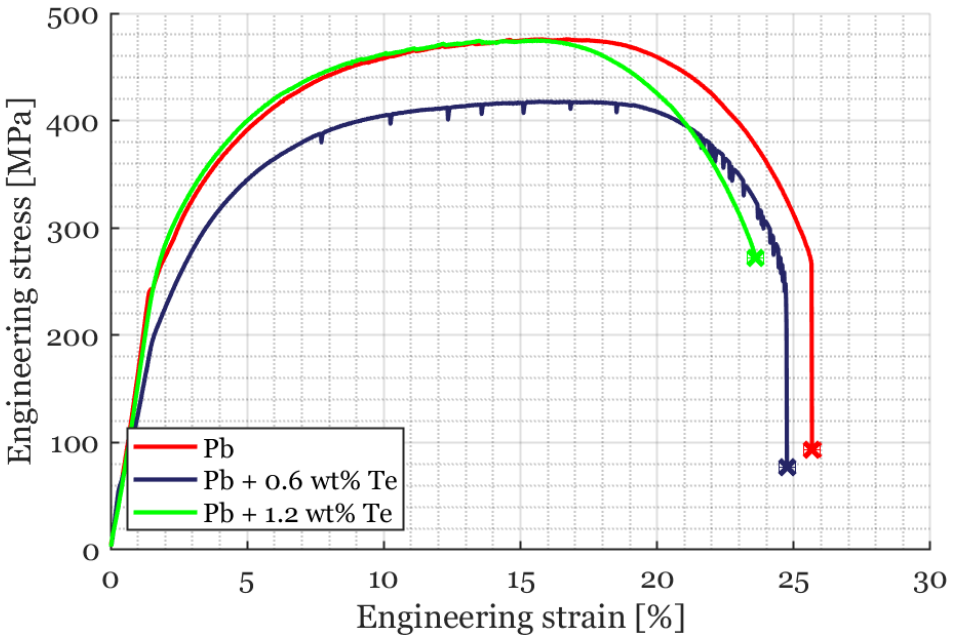

Figure 4.12: Stress-strain curves of unnotched 10-4 specimens in different environments at 375°C. R2 strain rate.

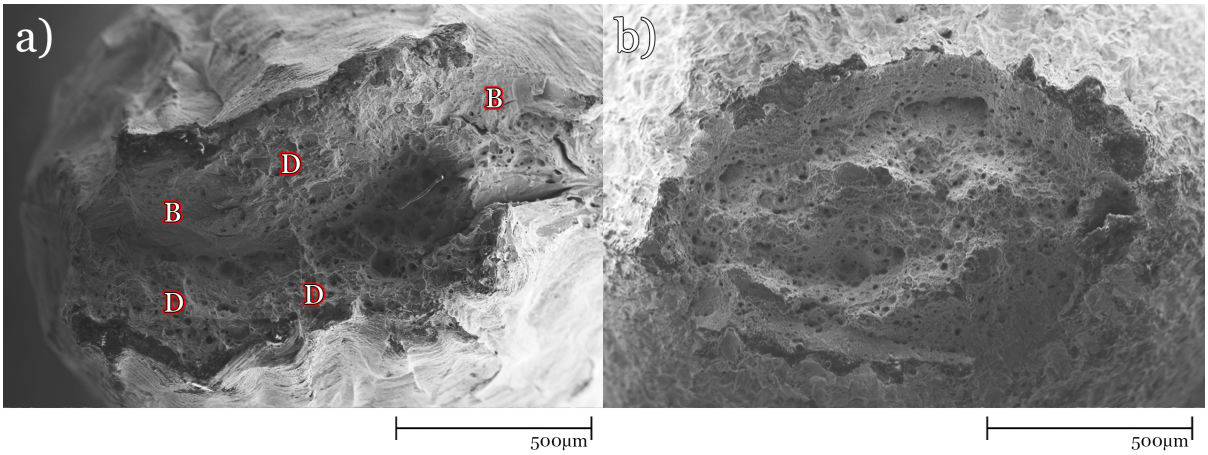

Figure 4.13: SEM picture of fracture surface of unnotched 10-4 specimens in Pb+Te at concentration a) 0.6%Te and b) 1.2 %Te. Both have been pulled at R2 and 375°C. ”B” and ”D” respectively mean ”brittle” and ”ductile” fracture appearance.

4.2 Notched Samples

As mentioned in chapter 3, only 10-4 steel has been tested with notched specimens. Tests of 10-4 steel conducted in a pure ArH_2 atmosphere, room temperature and 375°C, and in pure lead are compared; their corresponding stress-strain curves are shown in Figure 4.14. The samples tested in ArH_2 at 375°C exhibit both lower UTS and reduced elongation at fracture compared to those tested at room temperature in the same environment. The behavior of the specimen tested in lead closely resembles that of samples tested in ArH_2 at 375°C. The analysis of the fracture surfaces of specimens tested in an ArH_2 atmosphere showed no clear differences as test temperature increased. All samples displayed a fully ductile fracture, with clear dimples and strong necking. The same ductile behavior was also observed in samples tested at the same temperature in pure lead.

Tests on 10-4 steel performed in pure lead are compared to those with increasing reference Te concentrations. Their stress-strain curves are shown in Figure 4.15. The red curve represents the test conducted in pure lead. The dark blue curves correspond to tests with various Te concentrations and are plotted in the same color, as their relative differences do not stand out in this graph. The green and cyan curves refer to the tests at the lowest and highest Te concentrations used in this study, respectively. Both show almost identical behavior compared to the pure lead reference: similar UTS values and comparable fracture strain within typical experimental variation. In contrast, a completely different behavior is observed for the intermediate concentrations. These samples exhibit a sudden and premature drop in stress, as long as a relevant reduction in fracture strain. The total final elongation of the tests as a function of Te concentration is shown in Figure 4.16. The trend shows a decrease in fracture strain, reaching its minimum at 0.3 wt% Te, after which the value rises again, approaching the reference level at the highest concentration.

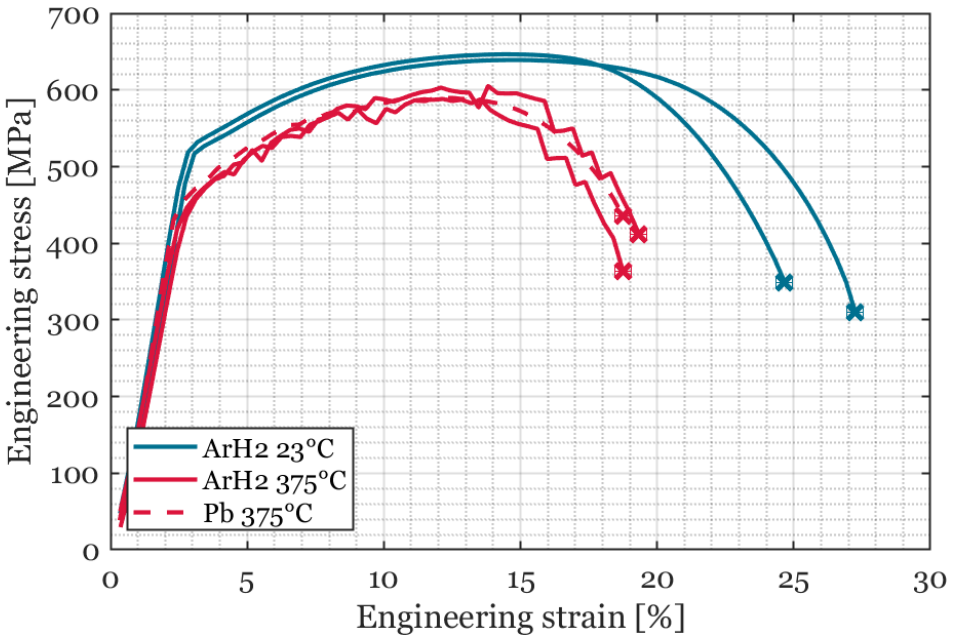

Figure 4.14: Stress-strain curves of reference notched 10-4 specimens. R1 strain rate.

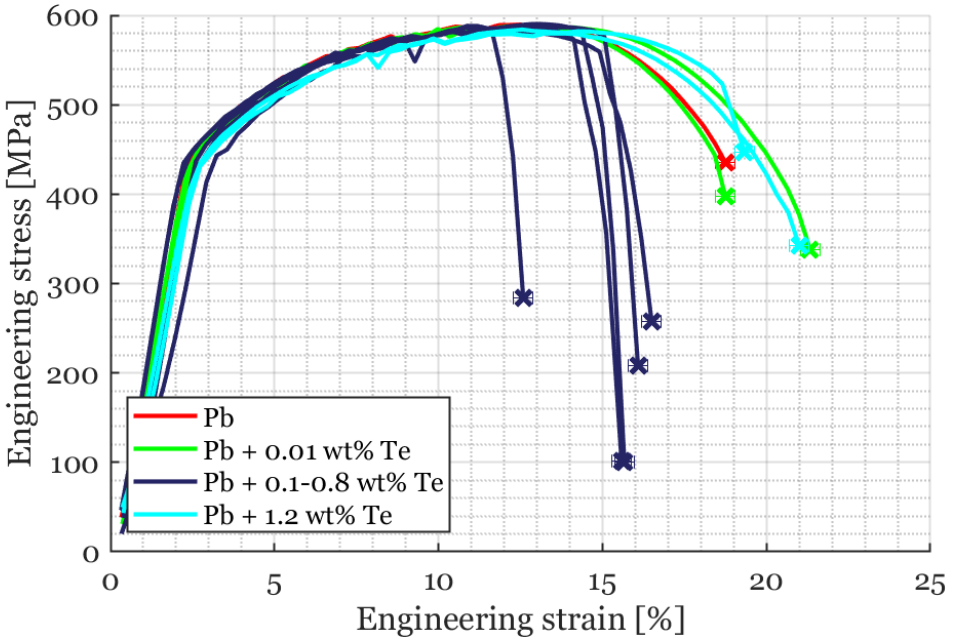

Figure 4.15: Stress-strain curves of notched 10-4 specimens at different Te concentrations. R1 strain rate.

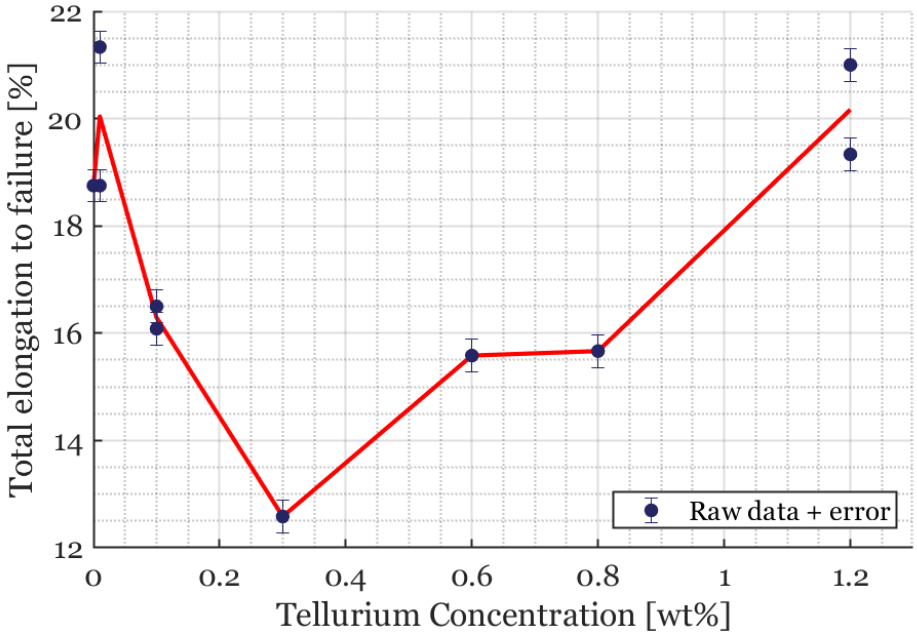

Figure 4.16: Total final elongation of notched 10-4 specimens tested in lead at 375°C with increasing tellurium concentration. R1 strain rate.

In Figure 4.17, SEM images of selected specimens from this batch are presented. The sample in pure lead exhibits clear features of ductile fracture. A similar behavior is observed in the sample with the lowest tellurium concentration, although a small area displays characteristics that differ from the main fracture surface. Specimens with intermediate tellurium concentrations show evident signs of brittle fracture propagation. The fracture initiation points are clearly identifiable: at the top side for the specimen with 0.3 wt% Te and on the left side for the one with 0.8 wt%. Propagation lines are distinctly visible, radiating from the initiation zones. The 0.8 wt% specimen also shows a localized region with ductile dimples. Finally, one of the specimens with 1.2 wt% Te displays the onset of a brittle fracture, with the initiation point highlighted in the magnified view. However, the crack propagation halts, and the remainder of the fracture surface presents typical ductile dimple features. The other specimen under the same conditions exhibits fully ductile-like fracture features.

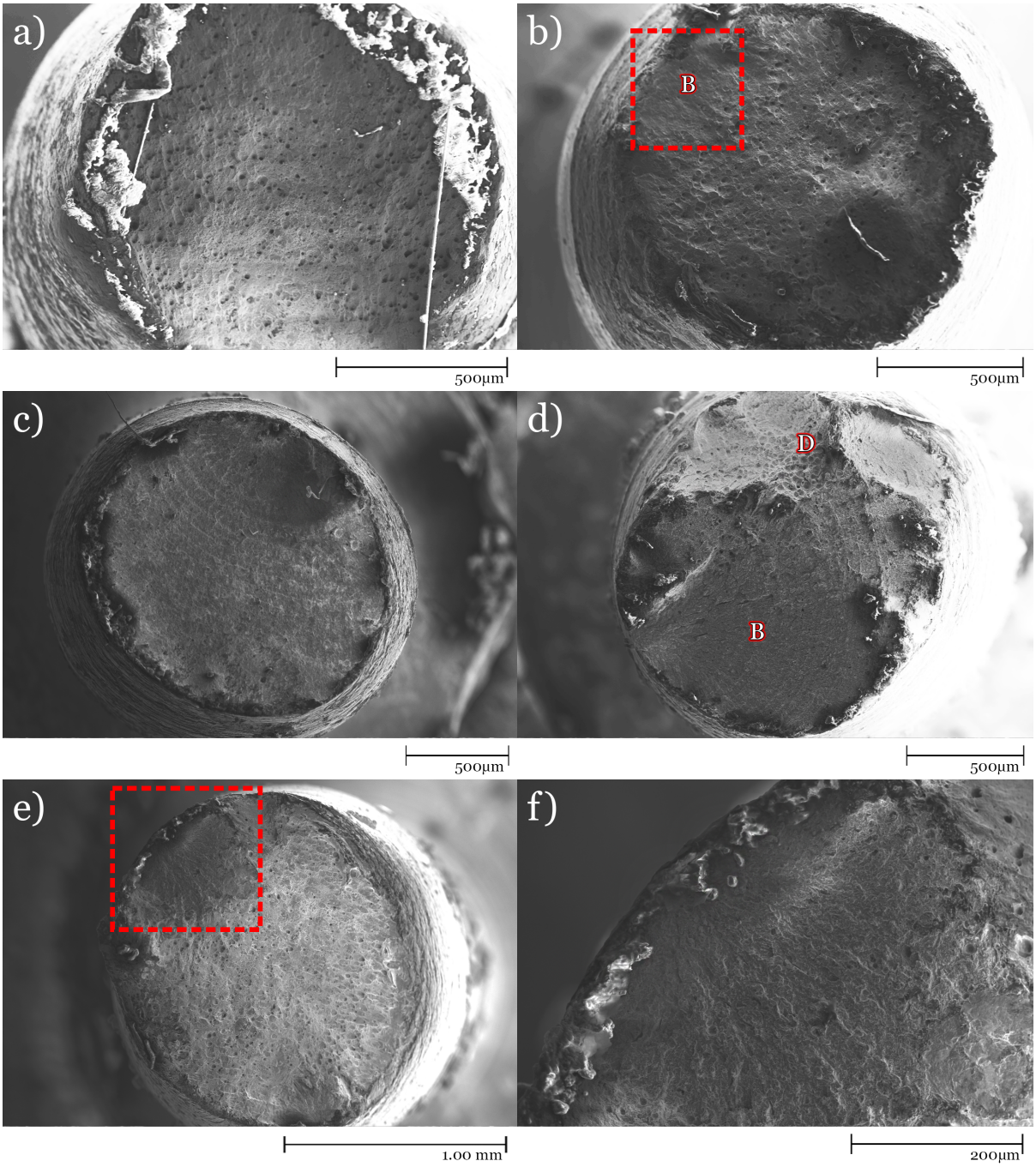

Figure 4.17: Fracture surfaces show necking formation in the different notched 10-4 samples, R1 strain rate in: a) pure Pb, b) Pb+0.01 wt% Te, the red box shows a probable brittle fracture feature, c) Pb+0.3 wt% Te , d) Pb+0.8 wt% Te, e) Pb+1.2 wt% Te and f) same as e) but zoomed on the red box. ”B” and ”D” respectively mean ”brittle” and ”ductile” fracture appearance.

4.3 Precipitates

In the samples with higher tellurium concentration, and generally in the tests conducted at higher temperatures, a significant amount of precipitates is visible in the SEM images. Their presence can be clearly seen, for instance, in Figure 4.3. However, to better observe and characterize these features, it is essential to analyze the images acquired using Backscattered Electrons (BSE), as these are sensitive to the elemental composition of the sample. An example is shown in Figure 4.18, where both an overview of the fracture surface of an unnotched sample tested in Pb + 1.2 wt% Te and a close-up detail are presented.

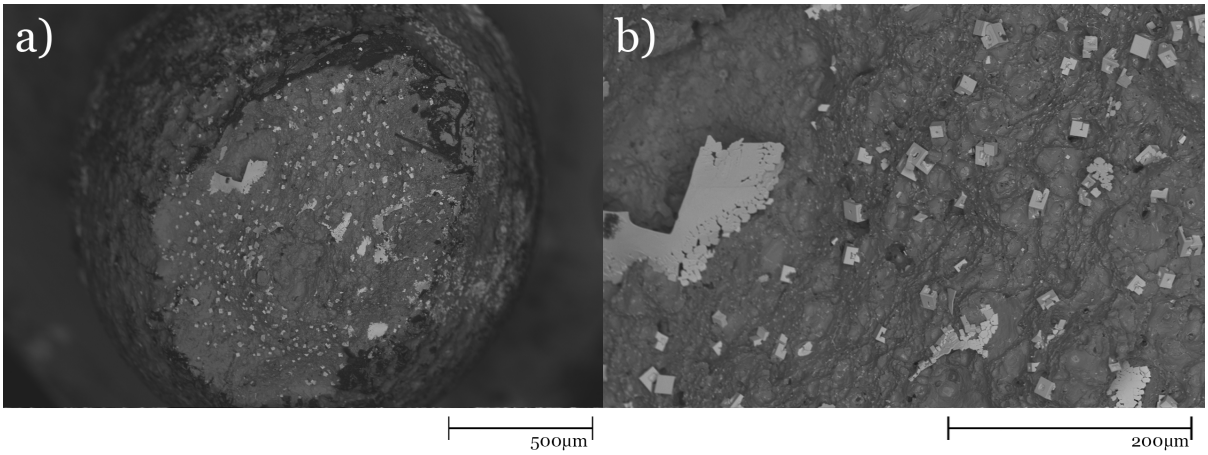

Figure 4.18: BSE-SEM images of an unnotched specimen tested in Pb + 1.2 wt% Te at 375°C, R1 strain rate. In a), the overall fracture surface is shown, while b) presents a close-up view.

The composition of the observed precipitates was analyzed using energy-dispersive X-ray spectroscopy (EDS). In Figure 4.19, selected points on a zoomed-in area of the fracture surface of a 316L specimen tested in Pb + 1.2 wt% Te at 550°C are analyzed. The atomic concentrations of the elements at each point are reported. The points located on the precipitates show comparable concentrations of tellurium and lead, which is consistent with the presence of lead telluride (PbTe). Additional analyses performed on similar precipitates in other samples yielded comparable results.

An EDS elemental map was acquired from a close-up of the fracture surface of sample 10-4, tested in Pb + 1.2 wt% Te at 375°C. The precipitates, which appear light gray in the SEM image, are composed of tellurium and lead, as shown by the corresponding elemental maps in Figure 4.20.

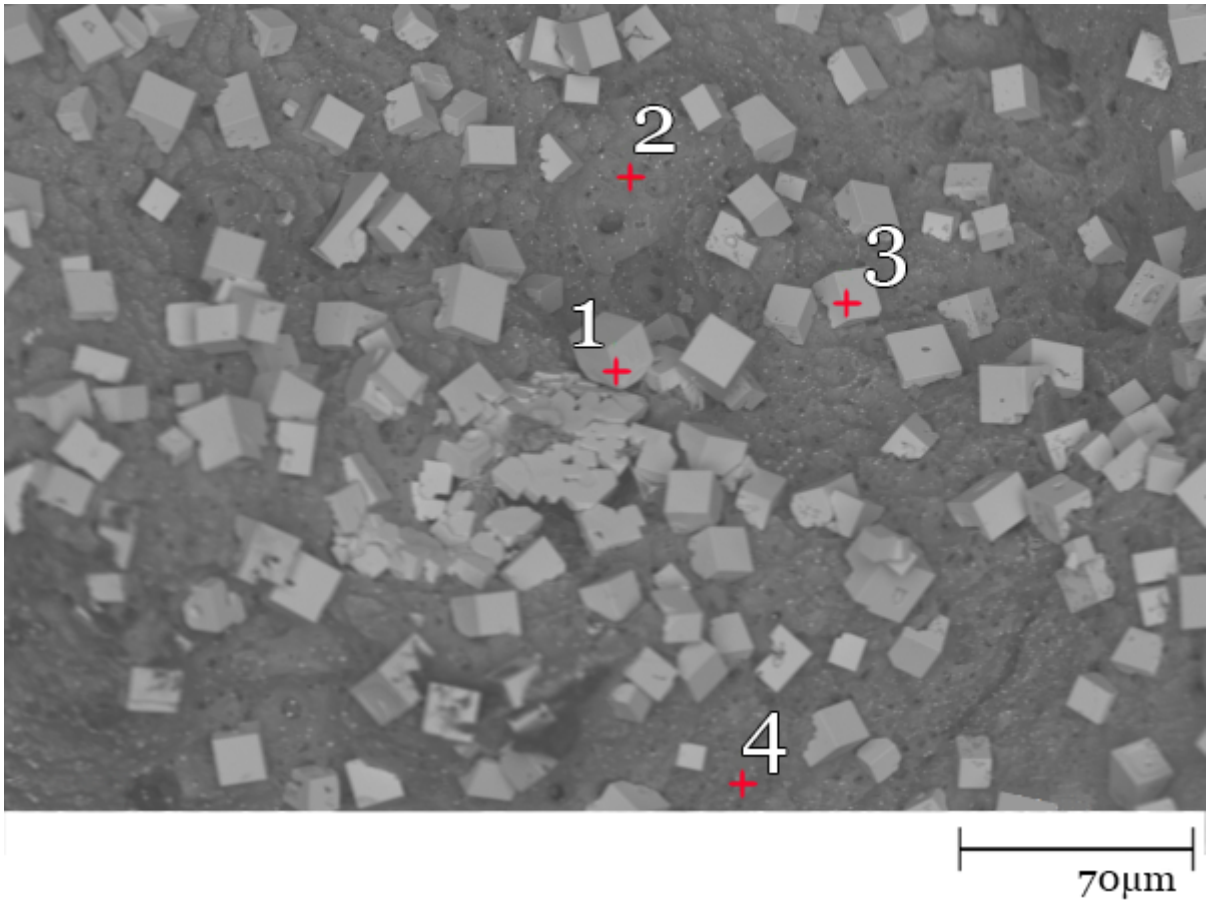

(a)

Element	#1	#2	#3	#4
Cr	5.35	20.56	5.90	15.73
Fe	13.39	70.93	13.73	77.47
Ni	1.34	7.36	3.18	4.63
Te	40.92	0.22	39.30	0.72
Pb	39.01	0.93	37.89	1.45

(b)

Figure 4.19: EDS analysis of 316L tested in Pb + 1.2 wt% Te at 550°C. (a) SEM close-up of the fracture surface showing a high concentration of precipitates. (b) Corresponding atomic% composition at the labeled points.

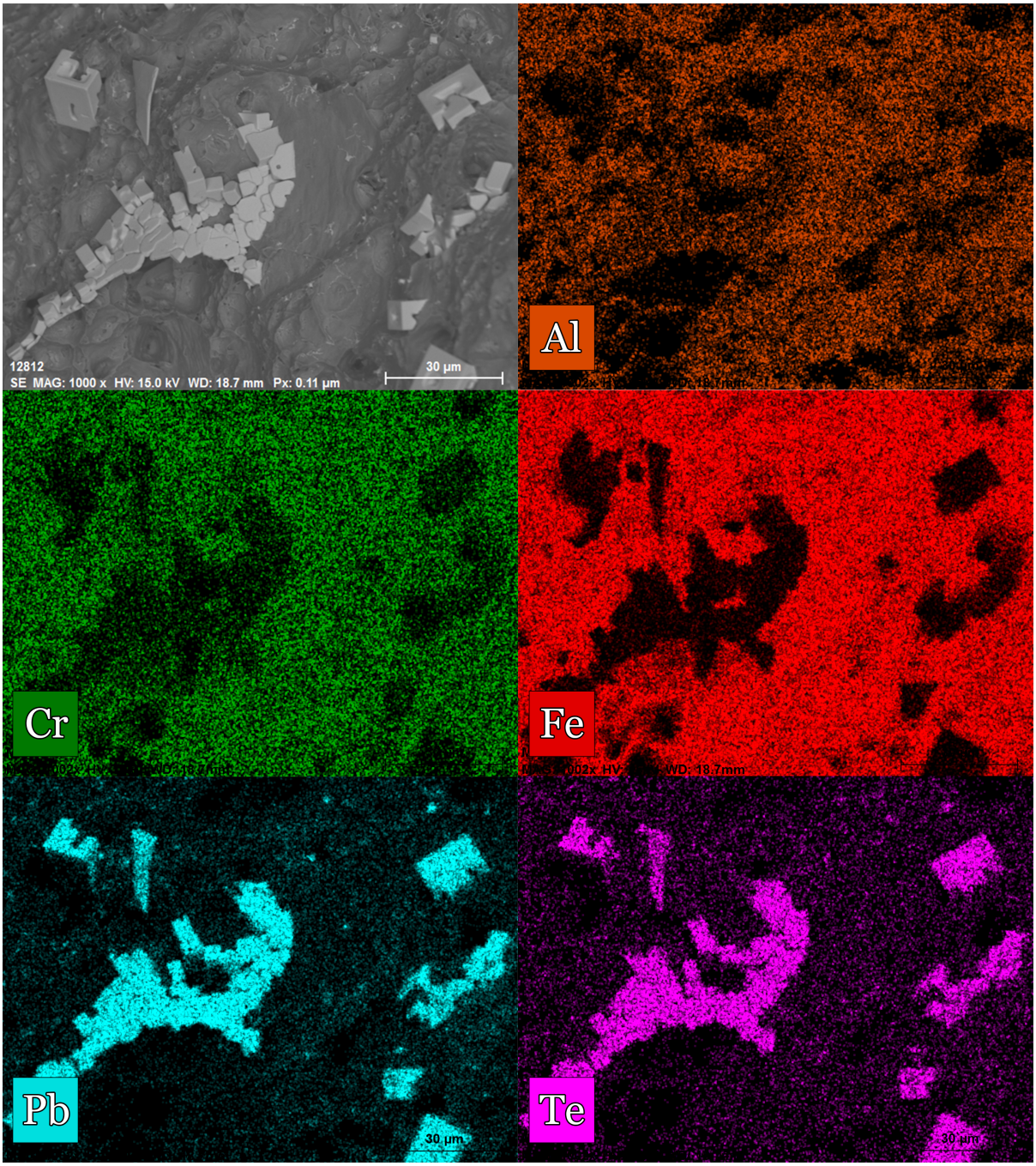

Figure 4.20: EDS map of close up on lead-tellurium precipitates of 10-4 unnotched sample tested in Pb+1.2 wt% Te at 375°C.

Figure 4.21: Solution precipitates observed in the area surrounding the specimen after opening the rig following the test of the notched sample in Pb+1.2 wt% Te.

Starting from the lower concentrations and increasing in intensity, a significant amount of precipitates was observed around the specimen, the U-bracket, and the drawbar when the rig was opened. As an example, Figure 4.21 shows the notched specimen tested in Pb + 1.2 wt% Te.

Chapter 5

Discussions and Conclusions

5.1 Discussions

Based on the obtained results, it can be concluded that the 10-4 steel is susceptible to LME in the presence of lead and tellurium. Stress concentrations, represented in this study by the presence of a notch, appear to intensify the embrittlement effect. This is likely due to the increased contact between the liquid and solid phases, which may reduce the stability and cohesion of the protective oxide layer. As the tellurium concentration increases, the embrittlement reaches its maximum severity at 0.3 wt% Te. Interestingly, full ductility is recovered at 1.2 wt% Te. This behavior may be related to a protective effect exerted by precipitates formed around the sample due to the supersaturated solution, which could act as a barrier, preventing direct interaction between the liquid metal and the solid material. A slower strain rate was found to mitigate the LME effect, suggesting a protective role. However, it remains unclear whether this improvement is due to the oxide layer having more time to adapt to the slower deformation, or to the increased time available for the formation of protective precipitates around the sample. It is important to highlight the general variability observed in the results. Two tests conducted under identical conditions may exhibit a final elongation difference of up to 5%. This strain variation is evident, for example, in the pure lead test curves shown in Figure 4.4 and Figure 4.6.

The following section provides a detailed analysis and discussion of each of these observations and hypotheses.

5.1.1 LME on Notched and Unnotched 10-4

The specimens tested at 375 °C in pure lead did not show any significant variation in fracture strain compared to those tested in ArH_2 atmosphere. This result is consistent with the findings reported in [23].

Dependence of LME Occurrence on Specimen Geometry

By analyzing only the unnotched specimens, it would seem premature to conclude that tellurium-induced embrittlement is present, as the reduction in fracture strain appears too small, as shown in Figure 4.7. However, comparing this with the corresponding plot for notched samples in Figure 4.16, it is evident that the trend is similar, showing a decrease that reaches a minimum at 0.3 wt% Te, followed by a recovery of ductility at 1.2 wt% Te. The aforementioned similarity can be observed in Figure 5.1, where the corresponding graphs are compared after normalization with respect to the engineering strain values measured in the reference lead condition for both cases. Additional specimens would be needed to improve the statistical significance of the observations, particularly for the unnotched samples, as the observed trend may be obscured by statistical dispersion. Nonetheless, it can be inferred that the presence of a notch amplifies the phenomenon. A plausible explanation is that the alumina scale, which forms around the sample due to sufficient oxygen concentration, is able to accommodate the imposed strain in unnotched specimens, thereby maintaining effective separation between the liquid metal and the bulk steel. In the case of notched samples, however, the stress concentration at the notch may be sufficient to overstress the oxide scale, preventing it from adapting to the deformation and thus from protecting the underlying steel effectively. The same is stated in [36], where unnotched T91 specimens did not undergo LME in pure lead, while the notched ones did.

Magnitude of LME

Assuming both specimen types exhibit the same trend in effects induced by LME, it is reasonable to jointly analyze the dependence of embrittlement magnitude on tellurium concentration. Starting from low tellurium concentrations up to 0.8 wt%, a clear reduction in maximum elongation is observed. One possible explanation lies in the fact that during pre-exposure, the maximum solubility of tellurium in lead is

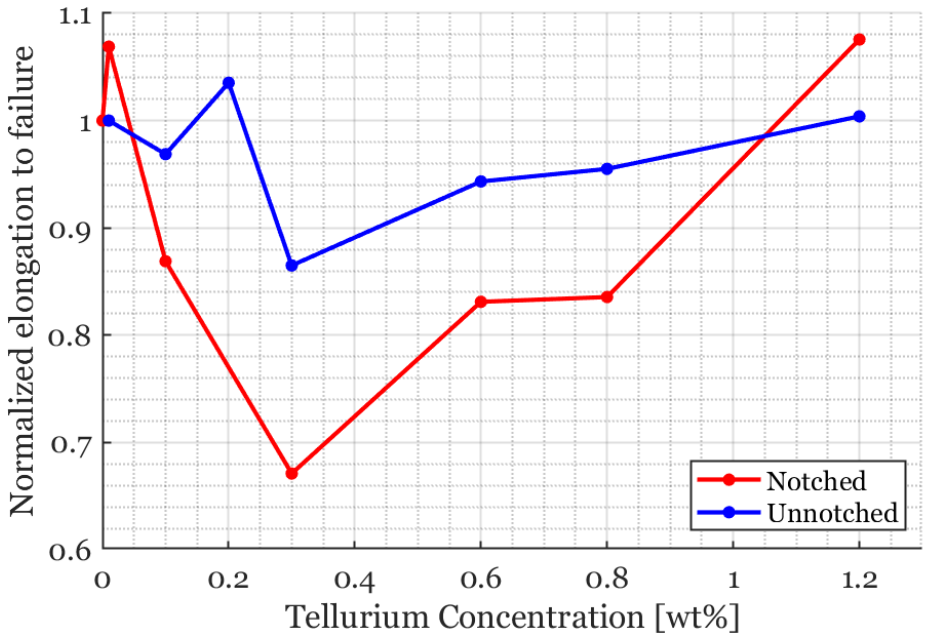

Figure 5.1: Engineering strain at fracture, normalized to the pure lead reference value, as a function of Te concentration for notched and unnotched specimens.

around 0.45 wt%. Therefore, when tests were conducted at similar concentrations (i.e., 0.6%, 0.8%), nucleation of precipitates was likely a slow and difficult process, in accordance with general kinetic principles. Thus, the 24-hour pre-exposure may not have been sufficient to saturate this process. As temperature was later reduced to 375 °C for testing, growth of precipitate crystals occurred simultaneously with additional nucleation points. This hindered the amount of precipitates formed in the chamber. Consequently, the solution remained oversaturated during testing compared to theoretical equilibrium, as tellurium did not have sufficient time to precipitate during cooling and testing phases. The limited presence of precipitates may have facilitated contact between liquid and solid phases. In contrast, for tests at 1.2 wt% Te, the solution was already supersaturated during the 24-hour pre-exposure. It can be assumed that all precipitates had sufficient time to form, and nucleation points developed throughout the chamber. As a result, when temperature was lowered for mechanical testing, nucleation had both time and favorable conditions to occur, making their growth much more likely. This probable presence of a greater amount of PbTe may have acted as a barrier, limiting direct contact between the liquid phase and the steel surface, as schematically shown in Figure 5.2. This behavior is consistent in both unnotched and notched specimens, as confirmed by SEM images in Figure 4.9 and Figure 4.17, respectively.

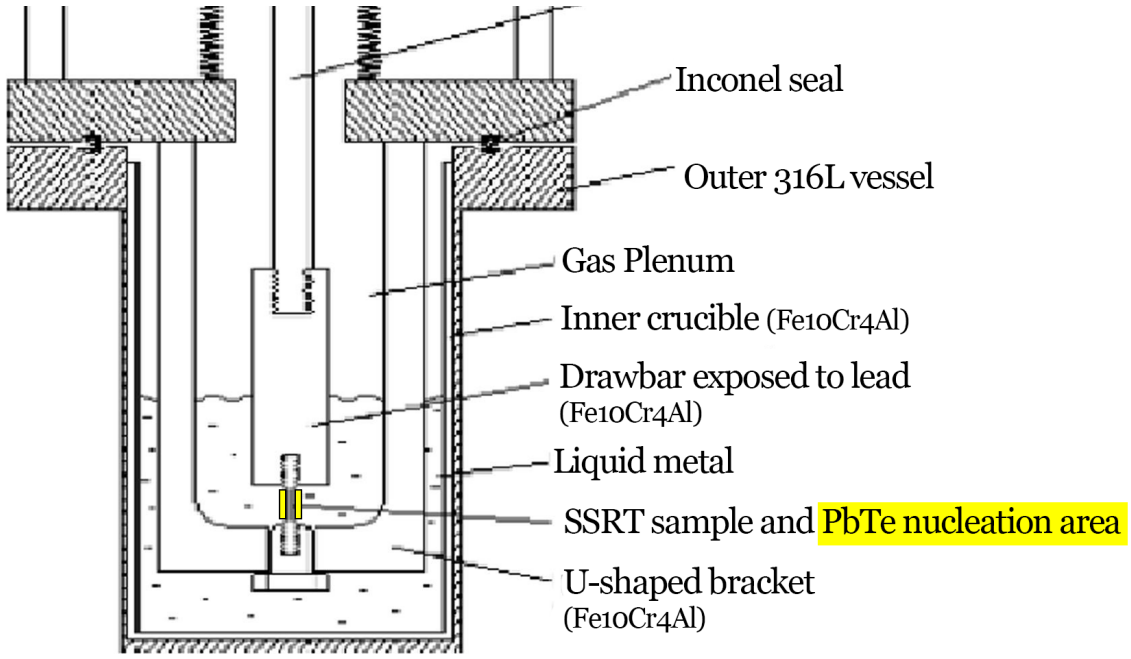

Figure 5.2: Schematic close-up of the SSRT rig and the formation of a precipitate barrier around the specimens, represented by the yellow area. Original picture from [23].

5.1.2 LME on Unnotched 10-4 at Slowest Strain Rate R2

Considering tests performed at R2, the only relevant and different behaviour is about the test conducted with 0.6 wt% Te. Its SEM image does not show any change in the fracture mode compared to the Pb reference test, as evidenced by the presence of dimples, as shown in Figure 4.13. When compared to the same specimen tested in the same environment but at strain rate R1, the difference is substantial, in that case the fracture brittle nature was clear. There are might be two explanations to such discrepancy: 1) this observation aligns with the discussion reported for the R1 tests, since the R2 test duration of 24 hours allowed the solution sufficient time to guarantee much higher amount of nucleation points at 375 °C and for all the tellurium that was supposed to precipitate to do so. Therefore, it is likely that the amount of precipitate formed was sufficient to prevent direct contact between the liquid phase and the steel; 2) the slower strain rate allowed the oxide to adapt and heal during specimen deformation, avoid close contact between the phases.

The following explains how to determine which of the two factors 1) or 2) played a more significant role in protecting the specimen. Considering that the test at R1 with 0.1 wt% Te primarily exhibited brittle fracture, as shown in Figure 4.9c), an additional test at R2 with 0.1 wt% Te should be performed. In such a case, the formation of precipitates can

not occur because the conditions are under saturation, so if no brittle features appear on the fracture surface, it would suggest that at lower strain rate the oxide performs better avoiding contact between solution and steel.

Moreover, tests at the R2 strain rate should be carried out across the entire range of tellurium concentrations using notched specimens. This is important to determine whether the slower strain rate can eliminate the reduction in fracture strain observed in notched specimens. This discrepancy for the very same test but at different strain rates can not be linked to the uncertainty in the tellurium concentration, as tests conducted at R1 show that brittle fracture occurs across a wide range of concentrations.

5.1.3 LME on 316L

Just like the 10-4 steel, the 316L alloy shows no signs of embrittlement in a molten lead environment containing 1.2 wt% tellurium. Additional tests should be carried out at intermediate concentrations, as was done for the 10-4 steel, to assess whether this alloy is also susceptible to LME.

5.1.4 Limitations of the Study

The main limitation of this study lies in the control of tellurium concentration. As discussed in chapter 3, the concentration was regulated with greater precision for notched samples compared to unnotched ones. Although it is not possible to define an exact error interval for the tellurium content, the formation of crystals on the rig was observed in both cases when the solubility limit was reached, providing an indirect confirmation of the concentration level.

Nevertheless, more precise control over the tellurium concentration should be pursued in future studies to improve reproducibility and accuracy. Despite this limitation, the outcomes and conclusions of this work are not compromised. This is because the core findings are based on observable trends and, most importantly, on the presence or absence of LME, which was clearly identified in this study.

5.2 Conclusions

The goal of this thesis was to **investigate the occurrence of embrittlement** and determine whether LME takes place under the studied conditions, as well as to identify the **critical tellurium concentration threshold** beyond which the mechanical properties of steel are significantly affected.

Based on both qualitative and quantitative analysis, it can be stated that a molten lead environment doped with tellurium at 375°C can embrittle ferritic 10-4 steel. In particular:

- Both unnotched and notched specimens show embrittlement behavior. At 375 °C, the strongest effect is observed at 0.3 wt% in both cases.
- The notch enhances the embrittlement, which is clearly visible from both the magnitude of fracture strain reduction and the SEM images.
- At concentrations far from the solubility limit at the pre-exposure temperature, embrittlement disappears—likely due to precipitate interaction and their kinetic formation.
- At lower strain rates (R2), the brittle fracture observed in the unnotched 10-4 sample tested at 0.6 wt% Te under higher strain rate conditions (R1) is no longer present. This may indicate a correlation with the timescale required for precipitate nucleation and growth, or with a more effective oxide protection mechanism under slower deformation.

5.2.1 Future Work

An interesting direction for future work is to investigate whether embrittlement also occurs at higher tellurium concentrations when testing at elevated temperatures—conditions under which the solubility of tellurium in lead is greater. In such cases, it would be possible to isolate the effect of the pure liquid solution, free from interference by solid precipitates, and assess whether LME (liquid metal embrittlement) still takes place. This approach would help clarify the role of precipitate formation in the apparent suppression of embrittlement observed at lower temperatures. However, it is also known that higher temperatures can mitigate or even eliminate the embrittling effect. Therefore, it would be equally valuable to investigate the extent to which

increasing temperature can suppress tellurium-induced embrittlement.

Another promising research direction would be to perform slow strain-rate tensile tests on notched specimens. Testing at lower strain rates may provide more insight into the mechanisms involved, potentially enhancing the visibility of embrittlement effects. These tests should be conducted at various tellurium concentrations—both below and above the solubility limit—to differentiate between effects caused by dissolved tellurium in the liquid phase and those influenced by the presence of solid precipitates.

Finally, it would be of interest to assess whether prolonged exposure of the alloy to a tellurium-containing environment results in a measurable reduction in total elongation. This would allow for the investigation of potential long-term corrosive effects of tellurium on the alloy, as suggested by previous studies such as [14], [12], [15], and [13].

5.2.2 Final Words

This research has highlighted the importance of studying the interaction between fission products and this promising steel, providing meaningful insight into the broader understanding of liquid metal embrittlement phenomena in next-generation reactor environments. Further in-depth investigation is necessary to better characterize the phenomenon under different conditions; however, the effect of tellurium dissolved in molten lead has now been clearly established.

Bibliography

[1] International Energy Agency, *World – energy mix*, Accessed: 2025-04-25, 2025.

[2] World Nuclear Association, *World nuclear association*, Accessed: 2025-04-25, 2025.

[3] B. Zohuri, "6 - generation iv nuclear reactors," in *Nuclear Reactor Technology Development and Utilization*, ser. Woodhead Publishing Series in Energy, S. U.-D. Khan and A. Nakhabov, Eds., Woodhead Publishing, 2020, pp. 213–246.

[4] American Public Power Association, *Nuclear renaissance*, Accessed: 2025-04-25, 2023.

[5] International Atomic Energy Agency, *Power reactor information system (pris)*, Accessed: 2025-04-25, 2025.

[6] World Nuclear Association. "Economics of nuclear power." Accessed: 2025-06-16, World Nuclear Association. (2024), [Online]. Available: `https://world-nuclear.org/information-library/economic-aspects/economics-of-nuclear-power#assessing-the-costs-of-nuclear-power`.

[7] N. Muellner, N. Arnold, K. Gufler, W. Kromp, W. Renneberg, and W. Liebert, "Nuclear energy - the solution to climate change?" *Energy Policy*, vol. 155, p. 112 363, 2021.

[8] Generation IV International Forum, *Generation iv international forum (gif)*, Accessed: 2025-04-25, 2025.

[9] Y. A. Kazansky, "0 - introduction to nuclear power technology," in *Nuclear Reactor Technology Development and Utilization*, ser. Woodhead Publishing Series in Energy, S. U.-D. Khan and A. Nakhabov, Eds., Woodhead Publishing, 2020, pp. 1–26.

[10] J. A. Hemsworth, M. G. Nicholas, and R. M. Crispin, “Tellurium embrittlement of type 316 steel,” *Journal of Materials Science*, vol. 25, no. 12, pp. 5248–5256, 1990.

[11] X.-W. Chu, H.-W. Cheng, C.-T. Fu, B. Leng, Y.-Y. Jia, F. Liu, and Z.-J. Li, “Effect of thermal exposure time on tellurium-induced embrittlement of ni–16mo–7cr–4fe alloy,” *Nuclear Science and Techniques*, vol. 28, no. 12, p. 178, 2017.

[12] M. Housseau, G. Dean, and F. Perret, “Behaviour and chemical state of irradiated ceramic fuels,” *Panel Proceedings Series*, p. 349, 1974.

[13] R. Lobb and I. Robins, “A study of the 20% cr/25% ni/nb stabilised stainless steel-tellurium reaction,” *Journal of Nuclear Materials*, vol. 62, no. 1, pp. 50–62, 1976.

[14] T. Yutani, S. Nomura, S. Koyama, Y. Kuwajima, and S. Ukai, “High temperature chemical reactions of fe-cr-ni and fe-cr cladding alloys by te, i2 and csoh/csi,” *Journal of Nuclear Materials*, vol. 201, pp. 35–45, 1993.

[15] O. Götzmann, P. Hofmann, and F. Thümmler, “Attack upon the cladding of oxide fuel pins by fuel and fission products,” *Journal of Nuclear Materials*, vol. 52, no. 1, pp. 33–50, 1974.

[16] Nuclear Energy Agency, *Handbook on Lead-bismuth Eutectic Alloy and Lead Properties, Materials Compatibility, Thermal-hydraulics and Technologies – 2015 Edition*. Paris: OECD Publishing, 2024, Originally published in 2015, updated edition.

[17] J. Zhang and N. Li, “Review of the studies on fundamental issues in lbe corrosion,” *Journal of Nuclear Materials*, vol. 373, no. 1, pp. 351–377, 2008.

[18] M. Miller, J. Hyde, M. Hetherington, A. Cerezo, G. Smith, and C. Elliott, “Spinodal decomposition in fe-cr alloys: Experimental study at the atomic level and comparison with computer models—i. introduction and methodology,” *Acta Metallurgica et Materialia*, vol. 43, no. 9, pp. 3385–3401, 1995.

[19] J. Hyde, M. Miller, M. Hetherington, A. Cerezo, G. Smith, and C. Elliott, “Spinodal decomposition in fe-cr alloys: Experimental study at the atomic level and comparison with computer models—ii. development of domain size and composition amplitude,” *Acta Metallurgica et Materialia*, vol. 43, no. 9, pp. 3403–3413, 1995.

[20] J. Hyde, M. Miller, M. Hetherington, A. Cerezo, G. Smith, and C. Elliott, "Spinodal decomposition in fe-cr alloys: Experimental study at the atomic level and comparison with computer models—iii. development of morphology," *Acta Metallurgica et Materialia*, vol. 43, no. 9, pp. 3415–3426, 1995.

[21] M. Gussev, K. Field, and Y. Yamamoto, "Design, properties, and weldability of advanced oxidation-resistant fecral alloys," *Materials Design*, vol. 129, pp. 227–238, 2017.

[22] P. Dömstedt, M. Lundberg, and P. Szakalos, "Corrosion studies of low-alloyed fecral steels in liquid lead at 750 °c," *Oxidation of Metals*, vol. 91, no. 3-4, pp. 511–524, 2019.

[23] C. Petersson, P. Szakálos, and D. Dietrich Stein, "Slow strain rate testing of fe-10cr-4al ferritic steel in liquid lead and lead–bismuth eutectic," *Nuclear Materials and Energy*, vol. 34, p. 101 403, 2023.

[24] P. Marcus, É. Protopopoff, and V. Maurice, "5 - surface chemistry and passivation of metals and alloys," in *Mechanics - Microstructure - Corrosion Coupling*, C. Blanc and I. Aubert, Eds., Elsevier, 2019, pp. 91–120.

[25] B. Scientific, *What is surface free energy?* Accessed: 2025-02-14, 2021.

[26] P. Moore and G. Booth, "8 - failure modes and analysis in metals," in *The Welding Engineer□s Guide to Fracture and Fatigue*, P. Moore and G. Booth, Eds., Oxford: Woodhead Publishing, 2015, pp. 95–110.

[27] A. Pineau and T. Pardoen, "Failure of metals," in *Comprehensive Structural Integrity (Second Edition)*, M. H. F. Aliabadi and W. O. Soboyejo, Eds., Second Edition, Oxford: Elsevier, 2003, pp. 321–432.

[28] D. McClements. "Ductile failure: Definition, causes, and prevention." Accessed: 2025-06-16, Xometry. (Mar. 2023), [Online]. Available: `https://www.xometry.com/resources/3d-printing/ductile-failure/`.

[29] T. A. Saleh, "Chapter 2 - adsorption technology and surface science," in *Surface Science of Adsorbents and Nanoadsorbents*, ser. Interface Science and Technology, T. A. Saleh, Ed., vol. 34, Elsevier, 2022, pp. 39–64.

[30] S. P. Lynch, "Liquid-metal embrittlement in an al 6%zn3%mg alloy," *Acta Metallurgica*, vol. 29, no. 2, pp. 325–340, 1981.

[31] M. KAMDAR, “Liquid metal embrittlement,” in *Embrittlement of Engineering Alloys*, ser. Treatise on Materials Science Technology, C. BRIANT and S. BANERJI, Eds., vol. 25, Elsevier, 1983, pp. 361–459.

[32] S. P. Lynch, “Metal-induced embrittlement of materials,” *Materials Characterization*, vol. 28, no. 3, pp. 279–289, 1992.

[33] P. Gordon, “Metal-induced embrittlement of metals—an evaluation of embrittler transport mechanisms,” *Metallurgical Transactions A*, vol. 9, pp. 267–273, 1978.

[34] J.-C. Lin, K.-C. Hsleh, R. C. Sharma, and Y. A. Chang, “The pb-te (lead-tellurium) system,” *Bulletin of Alloy Phase Diagrams*, vol. 10, no. 4, pp. 340–347, 1989.

[35] G. Müller, A. Heinzel, G. Schumacher, and A. Weisenburger, “Control of oxygen concentration in liquid lead and lead–bismuth,” *Journal of Nuclear Materials*, vol. 321, no. 2, pp. 256–262, 2003.

[36] A. Hojná, F. Di Gabriele, J. Klecka, and J. Burda, “Behaviour of the steel t91 under uniaxial and multiaxial slow loading in contact with liquid lead,” *Journal of Nuclear Materials*, vol. 466, pp. 292–301, 2015.

[37] J. Ejenstam, M. Halvarsson, J. Weidow, B. Jönsson, and P. Szakalos, “Oxidation studies of fe10cral–re alloys exposed to pb at 550°c for 10,000h,” *Journal of Nuclear Materials*, vol. 443, no. 1, pp. 161–170, 2013.

[38] X. Gong, F. Hu, J. Chen, H. Wang, H. Gong, J. Xiao, H. Wang, Y. Deng, B. Pang, X. Huang, Y. Li, and Y. Yin, “Effect of temperature on liquid metal embrittlement susceptibility of an fe10cr4al ferritic alloy in contact with stagnant lead-bismuth eutectic,” *Journal of Nuclear Materials*, vol. 537, p. 152 196, 2020.

[39] ZIROX. “Oxygen analyzer sgm5.” (2022), [Online]. Available: `https://www.zirox.de/en/products/analyzers/oxygen-analyzer-sgm5/`.

[40] J. Wallenius, *Fast Neutron Generation IV Reactors*. Unpublished manuscript, 2024, Textbook first draft, December 30, 2024.

Appendix - Contents

A Calculation of Engineering Strain and Uncertainty **62**

Appendix A

Calculation of Engineering Strain and Uncertainty

This appendix describes the method used to calculate the engineering strain and its associated uncertainty.

To compute the engineering strain, the following equation was used:

$$\varepsilon = 100 \cdot \frac{L_x}{L_{x_{\text{end}}}} \cdot \frac{L_{\text{end}} - L_{\text{ini}}}{l_{\text{ini}}} \tag{A.1}$$

where:

- L_x is the vector of positions occupied minute by minute by the drawbar,
- $L_{x_{\text{end}}}$ is the final position of the drawbar,
- L_{end} is the final total length of the specimen,
- L_{ini} is the initial total length of the specimen,
- l_{ini} is the initial gauge length of the specimen.

The first fraction uses data acquired from the software to weight the manually calculated fracture strain, represented by the second fraction. Each step of the strain evolution is therefore proportional to the final one, so the final reading from the software corresponds to the manually measured fracture strain.

Figure A.1: Close-up of the specimen halves reassembled after the test, ready for measurement.

In this formulation, the uncertainty of the engineering strain is only related to the measurements of the initial and final specimen lengths, both taken using a digital caliper.

It was observed through repeated measurements that the error in the initial length measurement does not exceed $\pm 0.02\,\text{mm}$, while the error in the final length measurement never exceeds $\pm 0.05\,\text{mm}$. The greater uncertainty in the final length arises from the need to realign the two broken halves of the specimen after testing, as illustrated in Figure A.1.

Assuming normally distributed measurement errors and a 99% confidence interval, the corresponding standard deviations are:

$$\sigma_{L_{\text{ini}}} = \frac{0.02\,\text{mm}}{2.576} = 0.00776\,\text{mm} \tag{A.2}$$

$$\sigma_{L_{\text{end}}} = \frac{0.05\,\text{mm}}{2.576} = 0.01940\,\text{mm} \tag{A.3}$$

The relative strain uncertainty (expressed in percent) was computed by propagating the independent uncertainties associated with L_{ini} and L_{end} using the following

equation:

$$\varepsilon_{\text{err}} = 2.576 \cdot 100 \cdot \frac{\sqrt{\sigma_{L_{\text{ini}}}^2 + \sigma_{L_{\text{end}}}^2}}{l_{\text{ini}}} \tag{A.4}$$

This expression represents the propagation of uncertainties assuming independent variables and provides the 99% confidence interval error in the engineering strain at the final measured point of the test.

This method ensures that the reported fracture strain values are accompanied by a realistic estimation of experimental uncertainty, in accordance with standard practice in mechanical testing.